

Spin period change and the magnetic fields of neutron stars in Be X-ray binaries in the Small Magellanic Cloud

H. Klus^{1*}, W.C.G. Ho², M.J. Coe¹, R.H.D. Corbet³ and L.J. Townsend¹

¹*Physics and Astronomy, University of Southampton, Southampton SO17 1BJ, UK*

²*Mathematical Sciences, University of Southampton, Southampton SO17 1BJ, UK*

³*University of Maryland Baltimore County, X-ray Astrophysics Laboratory, Mail Code 662, NASA Goddard Space Flight Center, Greenbelt, MD 20771, USA*

November 2013

ABSTRACT

We report on the long-term average spin period, rate of change of spin period and X-ray luminosity during outbursts for 42 Be X-ray binary systems in the Small Magellanic Cloud. We also collect and calculate parameters of each system and use these data to determine that all systems contain a neutron star which is accreting via a disc, rather than a wind, and that if these neutron stars are near spin equilibrium, then over half of them, including all with spin periods over about 100 s, have magnetic fields over the quantum critical level of 4.4×10^{13} G. If these neutron stars are not close to spin equilibrium, then their magnetic fields are inferred to be much lower, of the order of 10^6 – 10^{10} G, comparable to the fields of neutron stars in low-mass X-ray binaries. Both results are unexpected and have implications for the rate of magnetic field decay and the isolated neutron star population.

Key words: X-rays: accretion, accretion discs – stars: magnetic field – stars: neutron – pulsars: general – X-rays: binaries.

1 INTRODUCTION

X-ray binaries contain a compact star - a white dwarf, neutron star or black hole - and a mass donor companion. They are generally divided into two groups depending on the mass of their companion. Low-mass X-ray binaries (LMXB) contain a companion comparable in mass to the Sun or less, whilst high-mass X-ray binaries (HMXB) contain a companion star over 10 times the mass of the Sun (Grimm, Gilfanov & Sunyaev 2003). This is either a supergiant star - in the case of supergiant X-ray binaries (SGXB) - or an OBe star - in the case of Be X-ray binaries (BeXB). OBe stars are fast-rotating O- or B-type stars that show Balmer lines in emission, indicating the presence of a circumstellar disc. The compact star in all confirmed BeXB is a neutron star (Reig 2011), although there are several white dwarf candidates (Haberl 1995; de Oliveira et al. 2006; Sturm et al. 2012). BeXB typically have eccentric orbits and at periastron the neutron star briefly passes through the edge of the OBe star's circumstellar disc where it can accrete matter, either via a Keplerian accretion disc or via a wind, causing X-ray outbursts. An accretion disc can only form if the net angular momentum per unit mass of accreted matter is large enough (see Section 3). Once it is known how

the neutron star in each system accretes, then an appropriate theory of accretion can be used to determine its magnetic field based only on the long-term average spin period and X-ray luminosity (for disc accretion) or the long-term average spin period, X-ray luminosity, orbital period and relative velocity of accreted matter (for wind accretion). This assumes that the neutron stars in each system are near spin equilibrium with a rate of change of spin period near zero. Since we actually measure the rate of change of spin period (or determine upper limits in a few systems), we do not need to assume spin equilibrium, and we can obtain more rigorous results.

We use archival Rossi X-ray Timing Explorer (RXTE) data taken with the Proportional Counter Array to determine the long-term average spin period, rate of change of spin period and X-ray luminosity during outbursts for 42 BeXB in the Small Magellanic Cloud (SMC). We then determine the most likely magnetic field of the neutron star in each of these systems. This is the first time that the rate of change of spin period and the long-term average X-ray luminosity has been accurately measured for so many systems. The Magellanic Clouds provide astronomers with a valuable resource for studying BeXB because, not only do they provide whole galactic populations, but they are close enough for relatively faint optical sources to be resolved from the ground and they are at well-known distances and are rela-

* E-mail: hvk1g11@soton.ac.uk (HK)

tively un-observed by interstellar dust unlike most BeXB in the Milky Way.

An outline of the paper is as follows: our observations are discussed in Section 2. An evaluation of disc versus wind accretion is considered in Section 3. We briefly describe different models used to determine the magnetic field of the neutron star in Section 4, present our results in Section 5 and discuss possible consequences in Section 6.

2 OBSERVATIONS

The observations used in this paper come from the study of the SMC carried out using RXTE over the period 1997-2012. The SMC was observed once or twice a week and the activity of the neutron stars determined from timing analysis. See Laycock et al. (2005) and Galache et al. (2008) for detailed reports on this work; note that we report here on observations which extend the published record by several further years. As discussed in Laycock et al. and Galache et al., the quality of any single observation depends upon the significance of the detected period combined with the collimator response to the source. We remove any period detections with a significance less than 99%, a collimator response less than 0.2 (with the exception of SXP15.3 which reached a high enough X-ray luminosity to compensate for the low collimator value) and data sets with less than five detections. This leaves 42 systems with the number of detections between 5 and 88 (see Table 1). Fig. 1 shows the location of our sources.

The average count rate is converted to X-ray luminosity using

$$L = 0.4 \times 10^{37} \times 3 \times CR, \quad (1)$$

where we assume a distance of 60 kpc to the SMC and an average pulsed fraction of 33% (Coe, McBride & Corbet 2010). L is the X-ray luminosity in erg s^{-1} and CR is the RXTE count rate in counts/PCU/second. We then calculate a weighted \dot{P} by fitting the time evolution of the spin period using MPFITEXPR¹. [See the Appendix B for plots of P and L against Modified Julian Date (MJD) for all sources].

All $H\alpha$ measurements were obtained as part of the Southampton SMC X-ray binary pulsar (SXP) optical monitoring campaign that has been running for several years. The data were collected primarily at the South African Astronomical Observatory 1.9m telescope in South Africa and also at the ESO New Technology Telescope in Chile. The instrumental set-ups and the data reduction in both cases are the same as those described in Coe et al. (2012).

The orbital periods are mostly taken from Bird et al. (2012). We determine the relative velocity of accreted matter from the eccentricity of the system - which is known in six cases (Townsend et al. 2011b,a; Schurch 2009) and otherwise assumed to be 0.3 ± 0.2 , the $H\alpha$ equivalent width and the total mass of the system. The mass of the neutron star is assumed to be $1.4 M_{\odot}$ and we determine the mass of the OBe star from spectral type and luminosity class, mostly taken from McBride et al. (2008).

The values obtained for L , P , \dot{P} and the $H\alpha$ equivalent

width are shown in Table 1. The orbital period and eccentricity of each system are given in Table 2, as well as the spectral type, luminosity class, V band magnitude and the mass and radius of the OBe star in each system.

3 DISC OR WIND ACCRETION

From the parameters of each system, we determine whether each neutron star is accreting via a disc or wind. An accretion disc will form if the net angular momentum per unit mass of accreted matter J , is too large for it to accrete spherically or quasi-spherically. This occurs at the circularization radius R_{circ} , where

$$R_{\text{circ}} = \frac{J^2}{GM}. \quad (2)$$

Here G is the gravitational constant and M is the mass of the neutron star. If the neutron star and its magnetosphere are fully engulfed in the OBe star's circumstellar disc then

$$J = -\frac{1}{4}(n_{\rho} + 1/2)V_{\text{rel}}\frac{R_B^2}{a}; \quad (3)$$

if the OBe star's circumstellar disc is truncated so that only approximately half the neutron star's magnetosphere is exposed to accreting material at a time (as is illustrated in Fig. 2 and discussed in Reig et al. (1997), Negueruela & Okazaki (2001), Okazaki & Negueruela (2001) and Okazaki et al. (2002)) then

$$J_t = -V_{\text{rel}}R_B \left[\frac{2}{3\pi} + \frac{1}{8}(n_{\rho} + 1/2)\frac{R_B}{a} \right] \quad (4)$$

[see Appendix A for the derivation of equations (3) and (4)]. Here V_{rel} is the relative velocity of accreted matter, n_{ρ} depends on the density gradient and is taken to be 2.5 ± 0.5 and a is the semimajor axis of the system, which we determine using

$$a = \left[\frac{P_{\text{orb}}^2 G(M + M_{\text{OB}})}{4\pi^2} \right]^{1/3}, \quad (5)$$

where P_{orb} is the orbital period of the neutron star and M_{OB} is the mass of the OBe star. R_B is the Bondi radius given by

$$R_B = \frac{2GM}{V_{\text{rel}}^2}. \quad (6)$$

In order for matter to be accreted it must first penetrate the neutron star's magnetosphere. The radius of the neutron star's magnetosphere is approximately equal to the Alfvén radius R_A - which occurs where the magnetic pressure of the neutron star is balanced by the ram pressure of infalling matter - and is given by

$$R_A = \left(\frac{\mu^4}{2GM\dot{M}} \right)^{1/7}. \quad (7)$$

Here, μ is the magnetic moment of the neutron star ($\sim BR_{\text{NS}}^3$), where R_{NS} is the radius of the neutron star, assumed throughout to be 10 km. We assume a magnetic field in the range 10^7 - 10^{15} G, corresponding to $\mu \approx 10^{25}$ - 10^{33} G cm³. \dot{M} ($=LR_{\text{NS}}/GM$) is the mass accretion rate. Thus, disc accretion occurs if $R_{\text{circ}} > R_A$. This inequality can

¹ www.physics.wisc.edu/~craigm/idl/down/mpfitexpr.pro

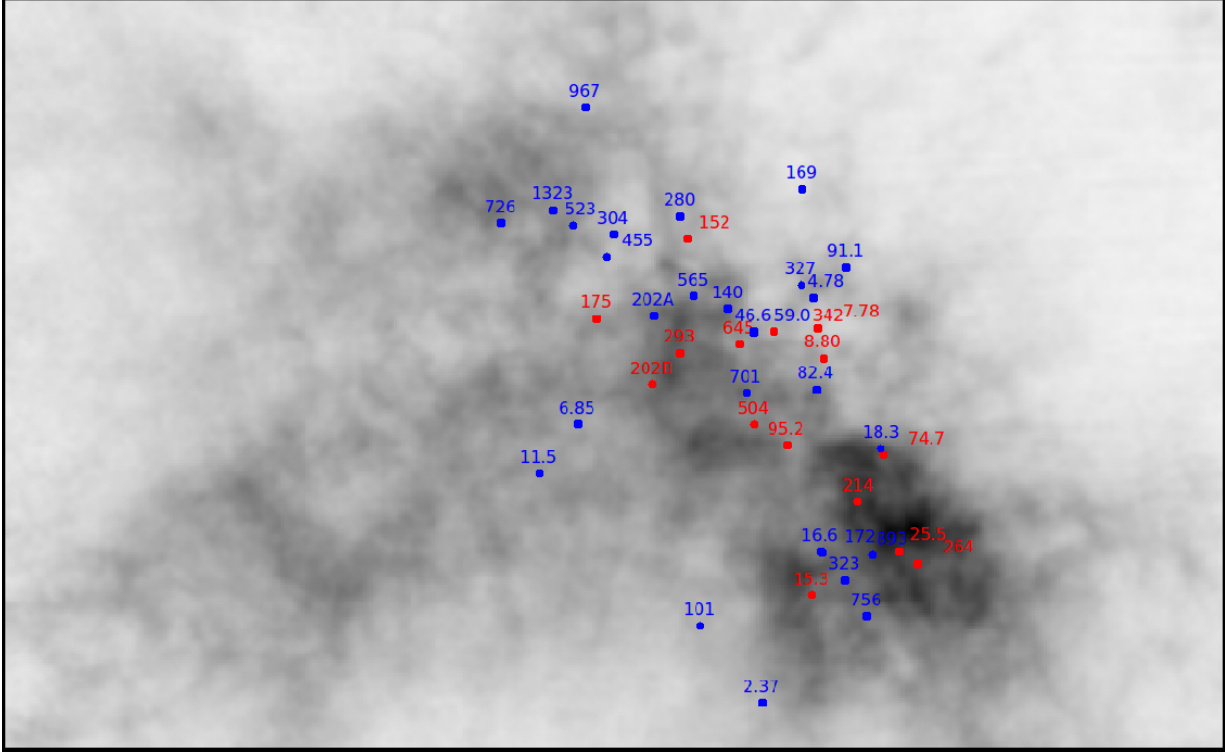


Figure 1. Image of the SMC from Stanimirović et al. (1999), taken by combining Parkes telescope observations of neutral hydrogen with an Australia Telescope Compact Array (ATCA) aperture synthesis mosaic, both in the radio spectrum. Neutron stars that are spinning up ($\dot{P} < 0$; blue circles) and down ($\dot{P} > 0$; red circles) are shown. Numbers indicate the spin period of each SMC X-ray binary pulsar (SXP).

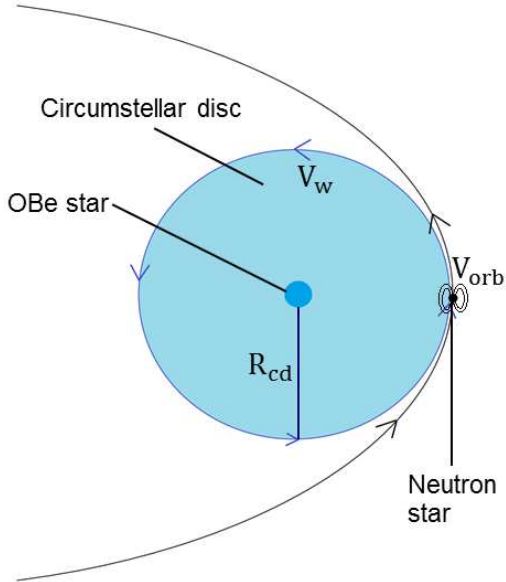


Figure 2. Schematic of the orbital system of a BeXB (not to scale). In this case the OBe star’s circumstellar disc is truncated by the neutron star orbit.

be rearranged to find the maximum relative velocity of accreted matter for which disc accretion can take place V_{Crel} . We determine V_{Crel} for each system using equations (2)-(7).

We determine the actual relative velocity of each system

using

$$V_{\text{rel}} = \sqrt{V_w^2 + V_{\text{orb}}^2 + 2V_w V_{\text{orb}} \cos\theta}, \quad (8)$$

where V_w is the velocity of accreted material, which we calculate by determining the stellar wind velocity at the radius of the OBe star’s circumstellar disc, R_{cd} . V_{orb} is the orbital velocity of the neutron star and θ is the angle at which the accreted material and neutron star impact, where $\theta=180^\circ$ indicates that the star and disc are in prograde motion. Some of these parameters are shown in Fig. 2. V_w is calculated by assuming that the circumstellar disc is in a circular orbit using;

$$V_w = \sqrt{\frac{GM_{\text{OB}}}{R_{\text{cd}}}}, \quad (9)$$

where R_{cd} is calculated using

$$\log\left(\sqrt{\frac{R_{\text{OB}}}{R_{\text{cd}}}}\right) = [-0.32 \times \log(-EWH\alpha)] - 0.2. \quad (10)$$

Here R_{OB} is the radius of the OBe star and $-EWH\alpha$ is the equivalent width of $H\alpha$ lines (in Angstrom), which are given in Table 1. V_{orb} is calculated using

$$V_{\text{orb}} = \sqrt{\frac{G(M + M_{\text{OB}})}{a} \frac{1+e}{1-e}}, \quad (11)$$

where e is the eccentricity of the system. Note that the above calculation estimates the velocity at a point and that the Bondi radius formally extends to infinity as the relative velocity becomes negligible. However even if the velocity difference across the Bondi radius is approximately V_w

BeXB	No. of detections	Range of data (yr)	Average P (s)	Average L (10^{37} erg s $^{-1}$)	Average \dot{P} (s yr $^{-1}$)	EW H α (Angstrom)
SXP2.37	24	11.22	2.37230 ± 0.00001	3.70 ± 0.06	-0.0036827 ± 0.0000003	-7.9 ± 0.6
SXP4.78	9	12.70	4.78015 ± 0.00004	0.71 ± 0.03	-0.00085 ± 0.00001	-43.7 ± 1.1
SXP6.85	61	8.03	6.85206 ± 0.00006	1.03 ± 0.02	-0.00022 ± 0.00001	-3.8
SXP7.78	29	12.30	7.7836 ± 0.0001	0.37 ± 0.01	0.00262 ± 0.00003	-14.3 ± 2.3
SXP8.80	46	11.23	8.89961 ± 0.00009	1.58 ± 0.02	0.001224 ± 0.000007	-5.1 ± 0.4
SXP11.5	18	0.15	11.4806 ± 0.0007	1.43 ± 0.04	-0.047 ± 0.006	
SXP15.3	10	11.13	15.2538 ± 0.0009	0.66 ± 0.03	0.0070 ± 0.0001	-25.1 ± 1.5
SXP16.6	12	5.46	16.555 ± 0.001	0.23 ± 0.01	-0.0131 ± 0.0005	
SXP18.3	74	7.39	18.3751 ± 0.0003	0.67 ± 0.01	-0.00118 ± 0.00006	
SXP25.5	35	10.56	25.5456 ± 0.0007	0.36 ± 0.01	0.0003 ± 0.0003	
SXP46.6	76	13.25	46.508 ± 0.003	0.45 ± 0.01	-0.0155 ± 0.0002	-21.9 ± 0.7
SXP59.0	88	13.10	58.859 ± 0.005	0.84 ± 0.02	-0.0206 ± 0.0005	-23.4 ± 1.4
SXP74.7	28	12.31	74.647 ± 0.008	1.10 ± 0.03	0.0300 ± 0.0004	-18.3 ± 2.3
SXP82.4	21	12.24	82.46 ± 0.02	0.50 ± 0.02	-0.022 ± 0.002	-25.9 ± 1.1
SXP91.1	59	13.48	88.38 ± 0.01	0.83 ± 0.01	-0.4417 ± 0.0006	-26.7 ± 2.6
SXP95.2	10	11.01	95.21 ± 0.04	0.63 ± 0.05	0.027 ± 0.005	
SXP101	5	13.32	101.77 ± 0.04	0.33 ± 0.04	-0.05 ± 0.01	-7.8
SXP140	5	6.67	140.4 ± 0.7	0.4 ± 0.1	-0.16 ± 0.10	-47.3 ± 3.1
SXP152	23	11.94	151.68 ± 0.06	0.39 ± 0.02	0.02 ± 0.01	-17.3 ± 1.7
SXP169	35	11.97	167.0 ± 0.1	0.69 ± 0.02	-0.238 ± 0.006	-29.2 ± 2.6
SXP172	42	10.39	171.86 ± 0.05	0.39 ± 0.02	-0.123 ± 0.006	-15.0 ± 1.3
SXP175	11	8.50	175.0 ± 0.1	0.50 ± 0.05	0.15 ± 0.01	
SXP202A	16	13.28	201.5 ± 0.1	0.50 ± 0.03	-0.13 ± 0.01	-18.1
SXP202B	5	13.24	202.3 ± 0.4	0.27 ± 0.05	0.21 ± 0.04	
SXP214	16	13.26	213.7 ± 0.1	0.29 ± 0.03	0.12 ± 0.02	
SXP264	6	10.13	262.6 ± 0.4	0.21 ± 0.03	0.06 ± 0.08	-30.1 ± 1.7
SXP280	6	8.24	280.0 ± 0.3	0.29 ± 0.05	-0.37 ± 0.06	-42.0 ± 3.1
SXP293	12	11.08	293.9 ± 0.3	0.28 ± 0.02	0.03 ± 0.05	
SXP304	7	6.09	304.1 ± 0.4	0.68 ± 0.09	-0.5 ± 0.2	-70.4 ± 6.2
SXP323	20	9.42	318.7 ± 0.2	0.55 ± 0.03	-0.95 ± 0.02	-30.9 ± 1.1
SXP327	5	1.76	327.5 ± 0.5	0.17 ± 0.02	-0.8 ± 0.8	
SXP342	20	10.29	341.0 ± 0.4	0.43 ± 0.03	0.96 ± 0.06	
SXP455	7	12.05	452.3 ± 1.3	0.7 ± 0.1	-0.2 ± 0.3	-15.1 ± 2.0
SXP504	31	13.29	502.0 ± 0.6	0.35 ± 0.02	0.34 ± 0.05	-52.9 ± 3.9
SXP565	8	7.48	564.1 ± 1.2	0.19 ± 0.04	-0.9 ± 0.4	-37.4 ± 2.9
SXP645	13	11.74	644.6 ± 2.2	0.25 ± 0.03	0.3 ± 0.3	
SXP701	27	11.71	695.8 ± 1.3	0.27 ± 0.02	-0.0 ± 0.3	-37.1 ± 3.5
SXP726	7	4.20	726.3 ± 4.1	0.48 ± 0.08	-1 ± 1	
SXP756	29	11.20	754.6 ± 0.8	0.63 ± 0.02	-0.01 ± 0.08	-27.0 ± 3.6
SXP893	29	10.44	890.8 ± 1.5	0.24 ± 0.02	-1.9 ± 0.3	
SXP967	7	2.85	962.9 ± 4.0	0.71 ± 0.09	-1 ± 3	-12.3
SXP1323	26	4.89	1323.7 ± 2.6	0.97 ± 0.04	-6.2 ± 0.7	-17.1 ± 1.5

Table 1. Long-term average spin period P, X-ray luminosity during outbursts L, rate of change of spin period \dot{P} , and H α equivalent width -EW H α , for all the systems in our data set satisfying the criteria described in Section 2. P, L and \dot{P} are obtained from RXTE data and H α measurements were obtained as part of the Southampton SXP optical monitoring campaign. Detections are defined as having a significance >99% and a collimator response of >0.2 (except in the case of SXP15.3 as discussed in Section 2).

$[\sim 140 \text{ km s}^{-1} (\text{M}_{\text{OB}}/15 \text{ M}_{\odot})^{1/2} (\text{R}_{\text{cd}}/150 \text{ R}_{\odot})^{-1/2}]$, we see that $V_{\text{w}}/V_{\text{Crel}} \lesssim 1$ when the disc is not truncated for most SXPs and $V_{\text{w}}/V_{\text{Crel}} < 0.3$ when the disc is truncated for all SXPs. More accurate results could be found using numerical simulations which are beyond the scope of this paper.

The critical relative velocity for disc accretion, V_{Crel} , and the actual relative velocity of each system, V_{rel} , are used to determine which systems in our data set contain neutron stars that accrete via a disc and which accrete via a quasi-spherical wind. We also determine the minimum possible angle that the neutron star's orbit must be misaligned with the OBE star's circumstellar disc for disc accretion to cease θ_{crit} , in both the truncated and non-truncated case, by rearranging equation (8) and using V_{Crel} in place of V_{rel} .

4 MAGNETIC FIELDS

We used three models applicable to disc accretion and two models applicable to wind accretion in order to determine the magnetic fields of the neutron star in each system. For spin equilibrium methods, see also Chashkina and Popov (2012).

4.1 Ghosh and Lamb model

The Ghosh and Lamb (1979) model is applicable to BeXB systems that contain neutron stars which accrete via a disc, whether or not they have achieved spin equilibrium (which entails a \dot{P} of zero and is discussed further in Section 4.2).

BeXB	P_{orb} (d)	Eccentricity	Spectral type & luminosity class	V_{mag}	M_{OB} (M_{\odot})	R_{OB} (R_{\odot})
SXP2.37	18.62 ± 0.02 [1]	0.07 ± 0.02 [4]	O9.5 III-V [13]	16.38 ± 0.02 [13]	19.9 ± 4.3	11.7 ± 5.3
SXP4.78	23.9 ± 0.06 [3]		B0-B1 V [10]	15.8 [10]	14.3 ± 3.5	6.6 ± 1.4
SXP6.85	21.9 ± 0.1 [4]	0.26 ± 0.03 [4]	O9.5-B0 IV-V [13]	14.59 ± 0.02 [13]	16.7 ± 2.9	7.2 ± 1.2
SXP7.78	44.93 ± 0.01 [2]		B1-B1.5 IV-V [13]	14.91 ± 0.02 [13]	12.2 ± 2.6	6.0 ± 1.2
SXP8.80	28.47 ± 0.04 [7]	0.41 ± 0.04 [4]	O9.5-B0 IV-V [13]	14.87 ± 0.12 [13]	16.7 ± 2.9	7.2 ± 1.2
SXP11.5	36.3 ± 0.4 [6]	0.28 ± 0.03 [11]	O9.5-B0 IV-V [11]	14.8 [13]	16.7 ± 2.9	7.2 ± 1.2
SXP15.3	74.32 ± 0.03 [2]		O9.5-B0 III-V [13]	14.67 ± 0.04 [13]	18.9 ± 5.1	11.3 ± 5.4
SXP16.6	33.72 ± 0.05 [7]					
SXP18.3	17.79 ± 0.03 [2]	0.43 ± 0.03 [12]	B1-B3 V [4]	15.6 [10]	10.7 ± 4.2	5.6 ± 1.6
SXP25.5	22.53 ± 0.01 [2]			15.2 [10]		
SXP46.6	137.4 ± 0.2 [2]		O9.5-B1 IV-V [13]	14.72 ± 0.03 [13]	15.2 ± 4.3	6.8 ± 1.6
SXP59.0	122.1 ± 0.38 [7]		O9 V [13]	15.28 ± 0.01 [13]	19.5 ± 2.0	7.8 ± 1.0
SXP74.7	33.387 ± 0.006 [2]	0.40 ± 0.23 [4]	B3 V [13]	16.92 ± 0.06 [13]	8.5 ± 2.0	4.9 ± 1.0
SXP82.4	362.3 ± 4.1 [7]		B1-B3 III-V [13]	15.02 ± 0.02 [13]	12.1 ± 5.6	8.7 ± 4.7
SXP91.1	88.37 ± 0.03 [2]		B0.5 III-V [13]	15.06 ± 0.06 [13]	16.1 ± 3.9	10.3 ± 4.8
SXP95.2	280 ± 8 [8]					
SXP101	21.949 ± 0.003 [2]			15.67 ± 0.15 [13]		
SXP140	197 ± 5 [5]		B1 V [13]	15.88 ± 0.03 [13]	12.9 ± 2.0	6.2 ± 1.0
SXP152			B1-B2.5 III-V [13]	15.69 ± 0.03 [13]	12.6 ± 5.2	8.9 ± 4.7
SXP169	68.37 ± 0.07 [2]		B0-B1 III-V [13]	15.53 ± 0.02 [13]	16.2 ± 5.4	10.4 ± 5.1
SXP172	68.78 ± 0.08 [2]		O9.5-B0 V [13]	14.45 ± 0.02 [13]	16.7 ± 2.9	7.2 ± 1.2
SXP175	87.2 ± 0.2 [9]		B0-B0.5 IIIe [9]	14.6 [9]	19.0 ± 3.0	14.5 ± 1.5
SXP202A	71.98 ± 5 [10]		B0-B1 V [13]	14.83 ± 0.02 [13]	14.3 ± 3.5	6.6 ± 1.4
SXP202B	224.6 ± 0.3 [2]		B0-5 III [10]	15.6 [10]	13.5 ± 8.5	11.5 ± 4.5
SXP214	4.5832 ± 0.0004 [2]		B2-B3 III [14]		11.9 ± 3.2	11.0 ± 1.7
SXP264	49.12 ± 0.03 [2]		B1-B1.5 V [13]	15.85 ± 0.01 [13]	13.7 ± 4.1	6.4 ± 1.6
SXP280	127.62 ± 0.25 [2]		B0-B2 III-V [13]	15.65 ± 0.03 [13]	14.9 ± 6.4	9.8 ± 5.3
SXP293	59.726 ± 0.006 [2]		B2-B3 V [10]	14.9 [10]	9.5 ± 3.0	5.2 ± 1.3
SXP304	520 ± 12 [5]		B0-B2 III-V [13]	15.72 ± 0.01 [13]	14.9 ± 6.4	9.8 ± 5.3
SXP323	116.6 ± 0.6 [7]		B0-B0.5 V [13]	15.44 ± 0.04 [13]	15.0 ± 2.8	6.8 ± 1.2
SXP327	45.93 ± 0.01 [2]			16.3 [10]		
SXP342						
SXP455	74.56 ± 0.05 [2]		B0.5-B2 IV-V [13]	15.49 ± 0.02 [13]	12.4 ± 3.9	6.1 ± 1.5
SXP504	270.1 ± 0.5 [2]		B1 III-V [13]	14.99 ± 0.01 [13]	14.5 ± 3.7	9.7 ± 4.5
SXP565	152.4 ± 0.3 [2]		B0-B2 IV-V [13]	15.97 ± 0.02 [13]	13.1 ± 4.7	6.3 ± 1.7
SXP645			B0-B0.5 III-V [10]	14.6 [10]	17.0 ± 4.8	10.7 ± 5.1
SXP701	412 ± 5 [10]		O9.5 V [13]	15.87 ± 0.05 [13]	17.5 ± 2.0	7.4 ± 1.0
SXP726			B0.5-B3 III-V [10]	15.6 [10]	12.9 ± 6.4	9.0 ± 5.0
SXP756	393.6 ± 1.2 [2]		O9.5-B0.5 III-V [13]	14.98 ± 0.02 [13]	18.0 ± 5.7	11.0 ± 5.4
SXP893	3.7434 ± 0.0005 [2]			16.3 [10]		
SXP967	101.4 ± 0.2 [2]		B0-B0.5 III-V [10]	14.6 [10]	17.0 ± 4.8	10.7 ± 5.1
SXP1323	26.174 ± 0.002 [2]		B0 III-V [13]	14.65 ± 0.02 [13]	17.9 ± 4.1	11.0 ± 5.0

Table 2. Orbital period P_{orb} , and eccentricity e , of each system in our data set. Also shown are the spectral type, luminosity class, V band magnitude and the mass and radius of the OBe star in each system. References are given in brackets and are as follows; 1 (Schurch, Udalski & Coe 2008), 2 (Bird et al. 2012), 3 (Coe et al. 2005), 4 (Townsend et al. 2011b), 5 (Schmidtke, Cowley & Udalski 2006), 6 (Townsend et al. 2009), 7 (Galache et al. 2008), 8 (Laycock et al. 2005), 9 (Townsend et al. 2013), 10 (Rajaelimanana, Charles & Udalski 2011), 11 (Townsend et al. 2011a), 12 (Schurch 2009), 13 (McBride et al. 2008), 14 (Coe et al. 2011).

This model predicts

$$-\dot{P} = 5.0 \times 10^{-5} \mu_{30}^{2/7} n(\omega_s) R_{\text{NS}6}^{6/7} \left(\frac{M}{M_{\odot}} \right)^{-3/7} I_{45}^{-1} (PL_{37}^{3/7})^2, \quad (12)$$

where \dot{P} is the rate of change of spin period measured in yr^{-1} , $\mu_{30} = \mu/10^{30} \text{ G cm}^3$, $I_{45} = I/10^{45} \text{ g cm}^2$, $R_{\text{NS}6} = R_{\text{NS}}/10^6 \text{ cm}$ and $L_{37} = L/10^{37} \text{ erg s}^{-1}$. $n(\omega_s)$ is the dimensionless accretion torque and depends on the fastness parameter ω_s . For $0 < \omega_s < 0.9$,

$$n(\omega_s) = 1.39(1 - (\omega_s[4.03(1 - \omega_s)^{0.173} - 0.878]))(1 - \omega_s)^{-1} \quad (13)$$

within 5% accuracy and

$$\omega_s = 1.35 \mu_{30}^{6/7} R_{\text{NS}6}^{-3/7} \left(\frac{M}{M_{\odot}} \right)^{-2/7} (PL_{37}^{3/7})^{-1}. \quad (14)$$

4.2 Kluzniak and Rappaport model

The Kluzniak and Rappaport (2007) model, like the Ghosh and Lamb model, is also applicable to BeXB systems that contain neutron stars which accrete via a disc, whether or

not they have achieved spin equilibrium. This model predicts

$$-\dot{P} = 8.2 \times 10^{-5} \mu_{30}^{2/7} g(\omega_s) R_{NS6}^{6/7} \left(\frac{M}{M_\odot}\right)^{-3/7} I_{45}^{-1} (PL_{37}^{3/7})^2, \quad (15)$$

where $g(\omega_s)$ is a function of the fastness parameter ω_s only and is of order unity; here we assume $R_0 \approx R_A$ for simplicity, where R_0 is defined in Kluzniak and Rappaport (2007). Note also small differences in definitions of R_A and ω_s between here and Kluzniak and Rappaport. In the spin equilibrium case, when $\omega_s \approx 1$,

$$B \approx 4.4 \times 10^{13} G R_{NS6}^{-3} \left(\frac{M}{M_\odot}\right)^{5/6} \dot{M}_{16}^{1/2} (P/100s)^{7/6}, \quad (16)$$

where $\dot{M}_{16} = \dot{M}/10^{16} \text{ g s}^{-1}$.

4.3 Equilibrium period model for disc accretion

The systems in our data set contain neutron stars which have relatively low rates of change of spin period and could be considered to be spinning close to their equilibrium period (see Section 5 for more details). Therefore, we also use a number of models which assume that the neutron stars in each system are close to spin equilibrium. The first of which is the equilibrium period model for disc accretion (Davidson & Ostriker 1973; Alpar et al. 1982).

As discussed in Section 3, accretion can only occur if matter is able to penetrate the neutron star's magnetosphere which is approximately at R_A . This can only happen if the neutron star, and hence its magnetosphere, are spinning slow enough; specifically, they must be spinning slower than the Keplerian velocity of matter that is corotating with the neutron star. The radius at which matter can corotate with the neutron star is known as the corotation radius

$$R_{co} = \left(\frac{GM P^2}{4\pi^2}\right)^{1/3}. \quad (17)$$

For accretion to occur, $R_{co} > R_A$. This generally causes the neutron star to spin up, $\dot{P} < 0$. If $R_{co} < R_A$, then matter is not accreted, but expelled by the centrifugal force of the neutron star in what is known as the propeller mechanism (Shvartsman 1970). This causes the neutron star to spin down, $\dot{P} > 0$.

If a system contains a neutron star which is in spin equilibrium, then it has a \dot{P} of 0, i.e. it is neither spinning up nor spinning down. This occurs when $R_{co} \approx R_A$ and so this equation can be rearranged to show the magnetic field of the neutron star in each system in terms of its X-ray luminosity - which is proportional to the mass accretion rate - and spin period, i.e.,

$$B \approx 1.8 \times 10^{13} G R_{NS6}^{-3} \left(\frac{M}{M_\odot}\right)^{5/6} \dot{M}_{16}^{1/2} \left(\frac{P}{100s}\right)^{7/6}. \quad (18)$$

Thus for systems with similar X-ray luminosities, as in the BeXB considered here, neutron stars with a higher spin period will have a higher magnetic field.

A similar result can be found with the equilibrium model for disc accretion (Pringle & Rees 1972). This determines the neutron star's magnetic field by considering accelerating and decelerating torques where, in the case of a star in spin equilibrium, these torques are balanced. The

spin up torque is equal to $\dot{M}\sqrt{GM\epsilon R_A}$ where ϵ is a numerical coefficient assumed to be 0.45 (Lipunov 1992). The spin down torque is equal to $\kappa_t \mu^2 / R_{co}^3$ where κ_t is a numerical coefficient assumed to be 1/3 (Lipunov 1992), i.e.,

$$\dot{M}\sqrt{GM\epsilon R_A} = \frac{\kappa_t \mu^2}{R_{co}^3}. \quad (19)$$

This yields

$$B \approx 1.4 \times 10^{13} G \left(\frac{\epsilon}{\kappa_t}\right)^{7/24} R_{NS6}^{-3} \left(\frac{M}{M_\odot}\right)^{5/6} \dot{M}_{16}^{1/2} \left(\frac{P}{100s}\right)^{7/6}. \quad (20)$$

4.4 Equilibrium period model for wind accretion

Wind accretion is possible if the system contains an OBe star with a non-truncated circumstellar disc and the neutron star's orbit is misaligned with the OBe star's circumstellar disc by an amount $> \theta_{crit}$. For this case, we use two models which assume accretion is occurring via a wind. The first model is the equilibrium period model for wind accretion (Illarionov & Sunyaev 1975; Illarionov & Kompaneets 1990) and is the same as the equilibrium model for disc accretion but with a different spin up torque. Here, the spin up torque is assumed to be $\dot{M}\eta\Omega_{orb}R_B^2$, where Ω_{orb} ($=2\pi/P_{orb}$) is the orbital frequency and η is a numerical coefficient assumed to be 1/4 (Lipunov 1992). B is then calculated using the following equation:

$$B \approx 1 \times 10^{14} G \left(\frac{\eta}{\kappa_t}\right)^{1/2} R_{NS6}^{-3} \left(\frac{M}{M_\odot}\right)^{3/2} \dot{M}_{16}^{1/2} \times \left(\frac{V_{rel}}{100 \text{ km/s}}\right)^{-2} \left(\frac{P/100s}{(P_{orb}/10d)^{1/2}}\right). \quad (21)$$

Here V_{rel} is measured in km s^{-1} , P_{orb} is measured in days and everything else in cgs units. Like the models for disc accretion, the magnetic field is proportional to the X-ray luminosity and spin period, but here it is also inversely proportional to the relative velocity of accreted matter and the orbital period of the system.

4.5 Shakura et al. model

The Shakura et al. model (see Postnov et al. 2011 and Shakura et al. 2012) applies to BeXB systems where accretion occurs via a wind and assumes that the neutron star is close to spin equilibrium. This model assumes that, in systems with slowly rotating neutron stars, matter forms an extended quasi-static shell around its magnetosphere which matter must pass through before being accreted. Postnov et al. (2011) find

$$B \approx 1 \times 10^{15} G R_{NS6}^{-3} \dot{M}_{16}^{1/3} \left(\frac{V_{rel}}{100 \text{ km/s}}\right)^{-11/3} \left(\frac{P/100s}{P_{orb}/10d}\right)^{11/12}. \quad (22)$$

5 RESULTS

We determine the long-term average X-ray luminosity during outbursts, spin period and rate of change of spin period for 42 BeXB systems in the SMC. The results which we

calculate from equations (2)-(12) are given in Table 3. A positive correlation is found between \dot{P} and P which follows a power-law with a slope of $\sim 4/3$, as is shown in Table 1 and Fig. 3; note that the Ghosh and Lamb model predicts a power law of 2 for slow rotators [see equation (12)]. There is also an asymmetry between the number of systems containing neutron stars that are spinning up and down, with 27 systems containing neutron stars that are spinning up on average and 15 systems containing neutron stars which are spinning down. Such a large proportion of spin down sources may indicate that these systems are close to spin equilibrium.

Fig. 4 shows a correlation between the neutron star spin period and the orbital period of the BeXB in our data set as would be expected from the Corbet relation (Corbet 1984). There is no apparent relationship between luminosity and either of these factors. However care should be taken as the instrument limitations of RXTE prevent the detection of luminosities below $\sim 10^{36}$ erg s $^{-1}$ (at the SMC distance). Given the uncertainty in relative velocities, we are unable to determine whether a correlation between velocity and luminosity exists, which would have provided an argument for very low relative velocities.

Fig. 5 shows the ratio of the relative velocity which we calculate using equation (8) and the critical relative velocity which we calculate using equations (2), (7) and either (3) or (4) against spin period. Equation (3) assumes that the neutron star and its magnetosphere are completely engulfed by the circumstellar disc during periastron and equation (4) assumes that, due to truncation of the OBe star's circumstellar disc, only half of the neutron star and its magnetosphere are exposed to the circumstellar disc at a time. In order for disc accretion to occur this ratio must be <1 . If this ratio is >1 , then accretion via wind becomes possible. It is clear from Fig. 5 that, whether the neutron star and its magnetosphere are completely engulfed by the circumstellar disc during periastron or not, all prograde systems are expected to contain neutron stars which accrete via a disc.

Fig. 5 shows that the systems in our data set are likely to contain neutron stars which are disc accreting. Therefore we consider models which assume disc accretion to be more appropriate. We also consider the disc accretion models which take \dot{P} into account to be more accurate. This applies to the Kluzniak and Rappaport and Ghosh and Lamb models. Fig. 6 shows the magnetic fields inferred from these models (using the measured P , \dot{P} and L for each BeXB). Results from the Ghosh and Lamb model are also given in Table 3. Both models predict two possible fields, where the higher magnetic fields are close to the magnetic fields predicted by spin equilibrium models which are shown in Fig. 7. Figs 6 and 7 show that the higher magnetic fields predicted by the Kluzniak and Rappaport and Ghosh and Lamb models, and all models which assume disc accretion and spin equilibrium, predict magnetic fields over the quantum critical level of 4.4×10^{13} G for all systems containing neutron stars with spin periods over about 100 s. This is over half of the systems in our data set. The lower fields predicted by the Kluzniak and Rappaport and Ghosh and Lamb models are all well below this value and are similar to those of neutron stars in LMXB. Unlike systems containing a neutron star which is close to spin equilibrium, the magnetic field in this case does not appear to depend on spin period.

Whilst disc accretion seems more likely, we also show in Table 3 the angle at which neutron star's orbit must be misaligned with the OBe star's circumstellar disc for disc accretion to cease in the non-truncated case. It is possible that this could happen - the OBe star could be tilted by the supernova that created the neutron star (Lai 1996) or the OBe star's circumstellar disc could be tilted due to radiation-induced warping (Pringle 1996) - and so we also determine the magnetic field using models for wind accretion assuming that these systems are in retrograde motion. If the circumstellar disc is truncated then wind accretion is not possible at any angle.

Fig. 7 shows that the models for wind accretion, specifically the equilibrium period model and the Shakura et al. model, predict lower magnetic fields than the models for disc accretion, assuming the systems contain a neutron star which is close to spin equilibrium, but still have systems containing neutron stars with fields over the quantum critical level. Incidentally, if these systems are wind accreting and in prograde motion then the predicted magnetic fields of their neutron stars would almost all be greater than the quantum critical level, with fields predicted to be as high as 10^{20} G.

Fig. 8 shows the magnetic field calculated by the Ghosh and Lamb model - and assuming the neutron stars in these systems are close to spin equilibrium - alongside magnetars, and neutron stars in Galactic BeXB that have had their magnetic fields determined from cyclotron resonance scattering features (CRSF; see below), plotted against spin period. If we were to plot the lower values from the Ghosh and Lamb model, then they would be situated far below the bottom of the plot and away from all other known sources (for further discussion of the systems in our data set in relation to other neutron star populations, see Ho et al. (2013)).

6 DISCUSSION AND CONCLUSIONS

We determine the long-term average spin period, rate of change of spin period and X-ray luminosity during outbursts for 42 BeXB in the SMC. All systems are expected to contain neutron stars which accrete from a disc, assuming that their orbital axis is not misaligned with the orbit of the OBe star's circumstellar disc by more than the values of θ_{crit} given in Table 3. If the neutron stars in these systems are close to spin equilibrium, then the magnetic field of over half, and all with spin periods over about 100 s, are over the quantum critical field $B_Q = 4.4 \times 10^{13}$ G. Note that similarly high estimates for the magnetic fields of neutron stars in binaries have been made before (see for example Lipunov (1992); Li & Van Den Heuvel (1999); Bozzo, Falanga & Stella (2008); Reig (2012); Klus et al. (2013)). If the systems containing neutron stars that are spinning up are not close to spin equilibrium, then some are predicted to have a much lower field. Both of these possibilities are unexpected when compared to the magnetic fields of neutron stars in Galactic BeXB measured using CRSF (see below).

Our work extends well-beyond that of Chashkina & Popov (2012) who derived magnetic fields of BeXB using some of the spin equilibrium models used here (see Section 4.1, 4.3-4.5), as well as others, but without accounting for the observed \dot{P} . They find similar results but arrive at dif-

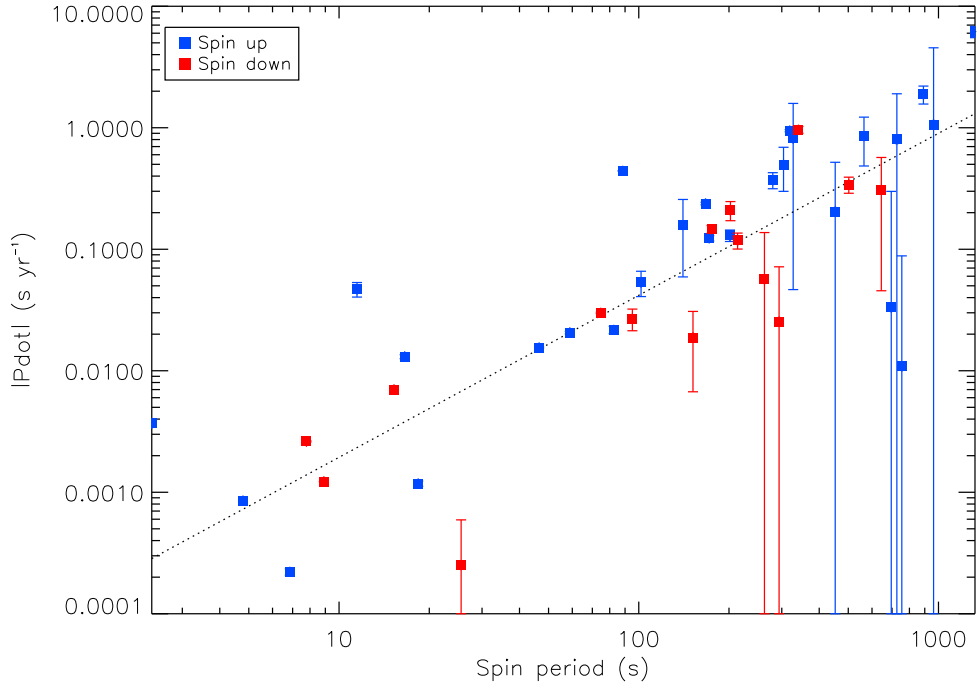


Figure 3. The long-term average rate of change of spin period \dot{P} , against spin period P , for neutron stars in the 42 BeXB in our data set: blue for $\dot{P} < 0$ (spin up) and red for $\dot{P} > 0$ (spin down). The dotted line indicates a correlation of $\dot{P} \propto P^{4/3}$.

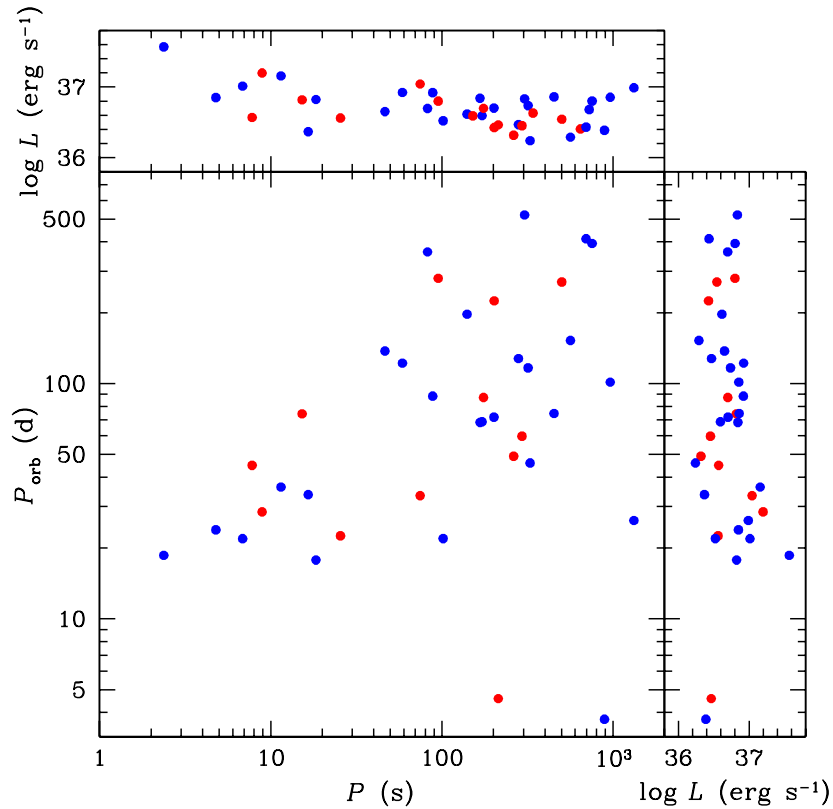


Figure 4. Corbet diagram (P_{orb} versus P) for the BeXB in our data set. Circles indicate neutron stars that are spinning up (blue) and spinning down (red). Error bars are not shown but are mostly smaller than the symbols.

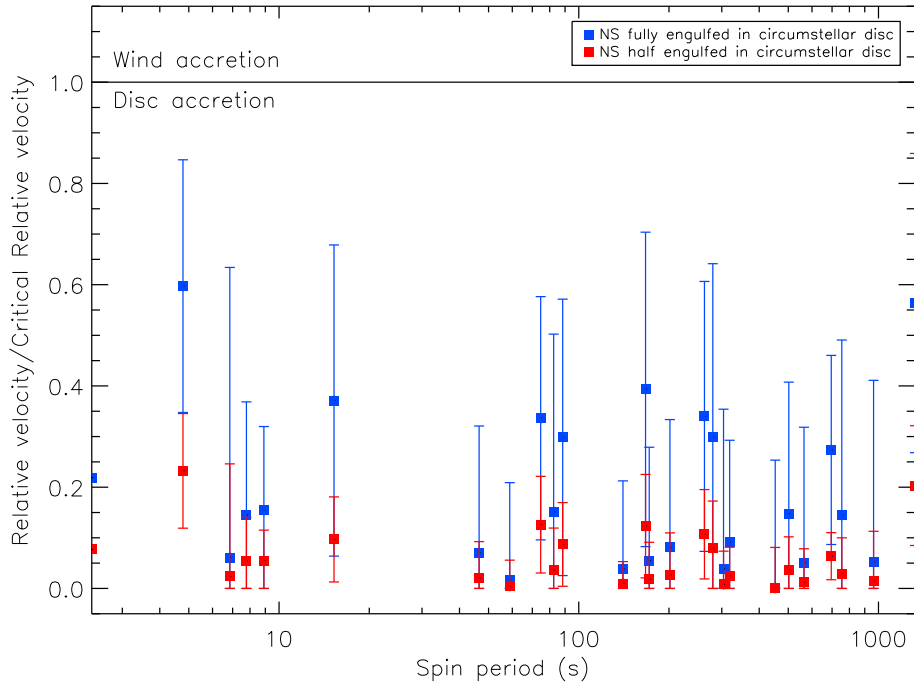


Figure 5. The ratio of relative velocity [equation (8)] and critical relative velocity [blue for equation (3) and red for equation (4)] versus spin period. Disc accretion occurs when this ratio <1 and wind accretion when this ratio >1 .

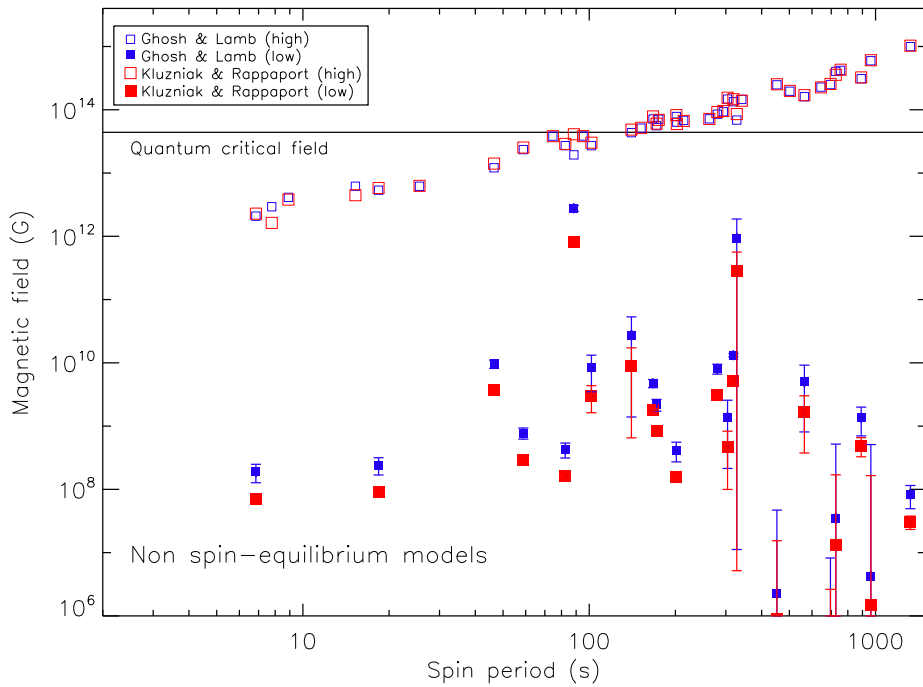


Figure 6. Neutron star magnetic field versus spin period determined using the Ghosh and Lamb (1979) and Kluźniak and Rappaport (2007) non-spin equilibrium models (see sections 4.1 and 4.2, respectively). The fact that there are two possible values, referred to as high and low, is discussed in Section 5. Errors bars for the higher values are not shown but are mostly the size of the symbols.

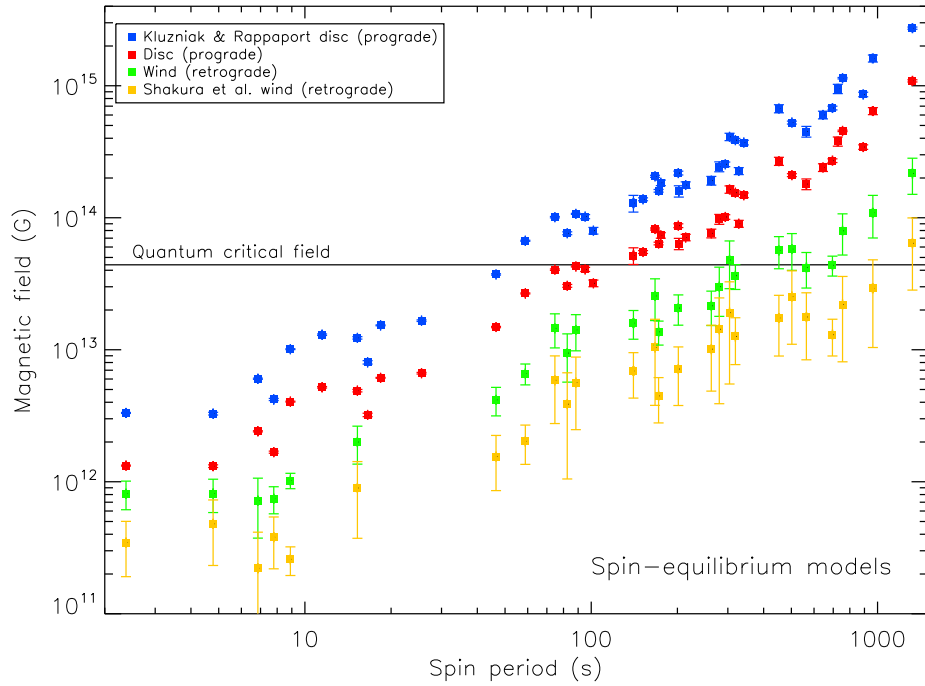


Figure 7. Neutron star magnetic field versus spin period determined using the spin equilibrium models discussed in Sections 4.2-4.5

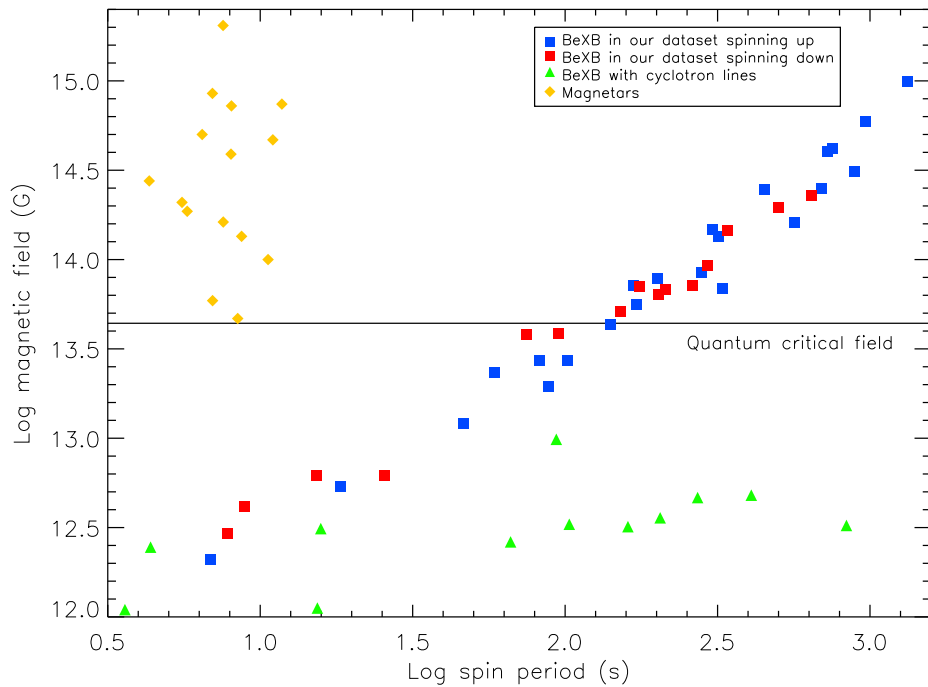


Figure 8. Magnetic field for the neutron stars in the BeXB in our data set which we calculate using the Ghosh and Lamb model and assuming these systems contain neutron stars which are close to spin equilibrium (blue for spin up and red for spin down). Also shown are BeXB whose magnetic fields are measured using cyclotron resonance scattering features (green) - where B and P are from; (Santangelo et al. 1999; Makishima et al. 1990; DeCesar et al. 2009; Heindl et al. 2001; Mihara et al. 1991; Shrader et al. 1991; Kendziorra et al. 1994; Heindl et al. 2003; Tsygankov et al. 2012; Klochkov et al. 2012; Doroshenko et al. 2010a; Coburn et al. 2001) - and magnetars (yellow) where P and \dot{P} are from Manchester et al. (2005) and B is determined from the standard $B=3.2 \times 10^{19} \text{ G} (P\dot{P})^{1/2}$ relation.

BeXB	$R_{\text{cd}}/R_{\text{OB}}$	V_{Crel} (km/s)	V_{Crel} (km/s) (truncated disc)	V_{rel} (km/s)	θ_{Crit} (degrees)	B (10^{12}G)	B (10^{10}G)
SXP2.37	9.4 ± 0.5	242 ± 27	687 ± 191	53 ± 52	68 ± 20		
SXP4.78	28.2 ± 0.5	219 ± 25	563 ± 155	131 ± 53	60 ± 46		
SXP6.85	6 ± 5	224 ± 25	577 ± 159	14 ± 128	49 ± 37	2.1 ± 0.4	0.019 ± 0.006
SXP7.78	14 ± 1	187 ± 21	496 ± 136	27 ± 42	62 ± 22	2.9 ± 0.5	
SXP8.80	7.1 ± 0.4	215 ± 24	607 ± 169	19 ± 35	47 ± 16	4.1 ± 0.7	
SXP11.5		203 ± 23	615 ± 172				
SXP15.3	19.8 ± 0.8	165 ± 19	632 ± 178	61 ± 50	59 ± 36	6 ± 1	
SXP16.6							
SXP18.3		240 ± 28	554 ± 152			5 ± 1	0.024 ± 0.007
SXP25.5						6 ± 1	
SXP46.6	18.1 ± 0.4	144 ± 16	502 ± 141	10 ± 36	58 ± 23	12 ± 2	1.0 ± 0.1
SXP59.0	18.9 ± 0.7	149 ± 16	557 ± 157	2 ± 29	56 ± 18	23 ± 4	0.08 ± 0.02
SXP74.7	16 ± 1	219 ± 25	583 ± 161	74 ± 52	72 ± 27	38 ± 7	
SXP82.4	20.2 ± 0.6	120 ± 14	507 ± 144	18 ± 42	68 ± 34	27 ± 6	0.04 ± 0.01
SXP91.1	21 ± 1	163 ± 18	559 ± 157	49 ± 44	66 ± 28	19 ± 4	278 ± 29
SXP95.2						38 ± 8	
SXP101	9 ± 4					27 ± 7	0.8 ± 0.5
SXP140	30 ± 1	135 ± 15	542 ± 153	5 ± 23	70 ± 17	43 ± 19	3 ± 3
SXP152	16 ± 1					51 ± 11	
SXP169	22 ± 1	171 ± 20	546 ± 153	67 ± 53	65 ± 37	71 ± 14	0.47 ± 0.07
SXP172	14.2 ± 0.8	166 ± 19	508 ± 142	9 ± 37	54 ± 21	56 ± 11	0.22 ± 0.05
SXP175		157 ± 17	512 ± 143			71 ± 16	
SXP202A	16.0 ± 3.0	169 ± 19	514 ± 144	14 ± 43	60 ± 24	78 ± 17	0.04 ± 0.01
SXP202B		128 ± 16	536 ± 153			64 ± 17	
SXP214		309 ± 35	525 ± 135			68 ± 16	
SXP264	22.2 ± 0.8	177 ± 20	561 ± 157	60 ± 47	61 ± 30	72 ± 19	
SXP280	27 ± 1	144 ± 17	543 ± 154	43 ± 49	68 ± 37	85 ± 24	0.8 ± 0.1
SXP293		178 ± 20	609 ± 171			93 ± 22	
SXP304	38.2 ± 2.2	110 ± 13	529 ± 151	4 ± 35	76 ± 29	148 ± 37	0.1 ± 0.1
SXP323	22.6 ± 0.5	151 ± 17	547 ± 154	14 ± 30	63 ± 19	134 ± 28	1.32 ± 0.08
SXP327		\pm	509 ± 142			69 ± 34	94 ± 94
SXP348	24 ± 1	153 ± 17	577 ± 167	27 ± 29	63 ± 19	146 ± 31	
SXP455	14 ± 1	173 ± 20	541 ± 152	0 ± 44	63 ± 23	248 ± 63	0.0002 ± 0.0045
SXP504	32 ± 2	123 ± 14	496 ± 141	18 ± 32	72 ± 24	196 ± 40	
SXP565	26 ± 1	138 ± 16	560 ± 159	7 ± 37	64 ± 25	161 ± 47	0.5 ± 0.4
SXP645						228 ± 59	
SXP701	25 ± 2	109 ± 12	467 ± 132	30 ± 20	53 ± 18	250 ± 53	0.0000003 ± 0.0008222
SXP726					\pm	404 ± 41	0.003 ± 0.048
SXP756	21 ± 2	114 ± 13	562 ± 160	17 ± 39	59 ± 36	419 ± 79	
SXP893						310 ± 69	0.13 ± 0.06
SXP967	13 ± 4	156 ± 18	569 ± 161	8 ± 56	58 ± 38	595 ± 150	0.0004 ± 0.0506
SXP1323	15.5 ± 0.9	213 ± 24	591 ± 164	120 ± 61	54 ± 28	996 ± 196	0.008 ± 0.003

Table 3. Ratio of the radius of circumstellar disc R_{cd} , over the radius of the OBe star in each system R_{OB} [see equation (10)], and the critical relative velocity for disc accretion which we determine using equations (2)-(7). Also shown are the relative velocities of each system which we determine using equation (8), where for disc accretion to occur, the relative velocity must be below the critical velocity, and the angle at which the neutron star's orbit must be misaligned with the OBe star's circumstellar disc for disc accretion to cease in the non-truncated case, which we determine using equations (2)-(6) and (10). The last two columns show the magnetic fields which we determine using the Ghosh and Lamb model.

ferent conclusions, in particular they favour the Shakura et al. wind accretion model (see Section 4.5), which produces magnetic fields that better match their population synthesis calculations (including magnetic field decay). As we showed in Section 5 (see Fig. 5), we find that it is more likely that the BeXB in our data set are accreting via a disc, rather than via a wind. This was derived (see Section 3) using the same disc versus wind accretion criteria as in Chashkina & Popov (2012), except we account for the pulsar interacting with the circumstellar disc of the OBe star near periastron passage (this has not been accounted for in previous works, see, e.g., Illarionov & Sunyaev 1975; Shapiro & Lightman 1976;

Wang 1981) and we evaluate the criteria using the measured system parameters for each BeXB. We also note that the population synthesis calculations performed in Chashkina & Popov (2012) assume a Ohmic magnetic field decay time-scale of 10^6 yr, as indicated by Pons et al. (2009). Our results suggest that the field decay time-scale is longer and therefore may still match population synthesis models with a longer time-scale.

12 Galactic BeXB contain neutron stars which have had their magnetic fields measured using cyclotron features. All have fields between 10^{12} - 10^{13} G (see Fig. 8) and they do not show the same correlation between magnetic field and

spin period that would be expected for systems containing a neutron star in spin equilibrium [see equations (16), (18), (20), (21) or (22)]. The lower fields for our data set, which we calculate from the Ghosh and Lamb model, are far lower than the magnetic fields of neutron stars in Galactic BeXB whose fields have been determined from cyclotron features ($\sim 10^6$ - 10^{10} G). The higher fields, which we also calculate using the Ghosh and Lamb model, are mostly much higher ($\sim 10^{12}$ - 10^{15} G) than the magnetic fields of neutron stars in Galactic BeXB which have been determined from cyclotron features. The values of the magnetic field determined for cyclotron line sources are closest to those predicted by the Shakura et al. model for systems in our data set that contain neutron stars which are wind accreting, orbiting OBe stars with a non-truncated circumstellar disc and in retrograde motion. However it is unlikely that this applies to most of our systems.

Another way to predict magnetic fields from our data set that are below the quantum critical level, and closer to the magnetic fields of neutron stars in Galactic BeXB, is to assume that the systems in our data set containing neutron stars with spin periods over 100 s have eccentricities larger than ≈ 0.8 . This would allow for wind accretion in prograde systems. The fields predicted from prograde quasi-spherical wind accretion with these eccentricities are below the quantum critical level. However Townsend et al. (2011a) show that no known BeXB system containing neutron stars with spin periods above 100 s have eccentricities above 0.5. There are four known BeXB with eccentricities above 0.8: three have spin periods below 1 s and one has a spin period of 94.3 s. Four of the cyclotron line sources have known eccentricities - two of which have spin periods above 100 s - and all are below 0.5.

For the sources whose magnetic field has been measured by CRSF, we can use their known values of P , L and \dot{P} and the models discussed in Section 4 to cross-check this magnetic field. This is currently possible for five sources: GRO J1008-57 (Shrader et al. 1991), A0535+26 (Kendziorra et al. 1994; Maisack et al. 1997), RX J0440.9+4431 (Tsygankov et al. 2012), 1A1118-616 (Doroshenko et al. 2010a; Nespoli & Reig 2011) and X Per (Coburn et al. 2001), whose magnetic fields are given in Table 4. Assuming that the neutron stars in these systems are disc accreting and close to spin equilibrium, then all models predict higher fields than those determined by the cyclotron features. The model which predicts magnetic fields closest to those determined by CRSF is the Shakura et al. model for systems containing a neutron star which is wind accreting from a non-truncated circumstellar disc and in retrograde motion, though it seems unlikely that this applies to all 12 of the CRSF systems. The magnetic fields predicted by the Ghosh and Lamb model are shown in Table 4. If the magnetic fields predicted by the Ghosh and Lamb model are taken to be the magnetic field at the surface of the neutron star and the CRSF gives the magnetic field of the accretion column, then the column would have to be 4 – 30 km above the surface (assuming $B \propto r^{-3}$), where the height for each source is shown in Table 4. A similar difference in field determination has previously been noted for SGXB GX 301-2 (Doroshenko et al. 2010b). It has also been observed that cyclotron lines may not be a true indicator of the surface magnetic field of neutron stars since different values

can be measured at different times, with these values sometimes changing rapidly (Reynolds, Parmar & White 1993; Staubert et al. 2007).

Becker et al. (2012) show that different heights of the accretion column can be determined depending on whether or not the X-ray luminosity is above a critical value (\sim a few $\times 10^{37}$ erg s $^{-1}$). The BeXB containing neutron stars that have had their fields measured with cyclotron features mostly have X-ray luminosities which are lower than this, and therefore the height of the accretion column should be inversely proportional to the X-ray luminosity. The heights calculated using the equations given by Becker et al. are between ~ 0.1 and 2 km from the surface except in the case of X Per where the height is ~ 9 km from the surface (see Table 4). In order to obtain the required height to reconcile the two magnetic field determinations for each source, the X-ray luminosity of the neutron star must be less than $\sim 10^{34}$ erg s $^{-1}$. However Poutanen et al. (2013) suggest that this issue may be more complex, with the CRSF from a single source changing due to the fact that the CRSF can originate from radiation that is produced by the accretion column and reflected from the neutron star's surface rather than from an accretion column that is changing heights. Although it is currently unclear why the values predicted using the Ghosh and Lamb model are so different to those determined by cyclotron features, future work in this area would help resolve the matter.

The wide range of magnetic fields may be caused by different mechanisms for forming neutron stars e.g. as a result of an electron capture supernova (Nomoto (1984); Podsiadlowski et al. (2004)) or accretion induced collapse (Nomoto (1984); Taam & van den Heuvel (1986); Nomoto & Kondo (1991)). If over half the neutron stars in systems in our data set do have fields over the quantum critical value then this could mean that magnetic field decay occurs more slowly than previously thought (Pons, Miralles & Geppert 2009). It may also mean that half the isolated neutron star population also have fields this high and are currently not observed due to selection effects.

ACKNOWLEDGEMENTS

We would like to thank the anonymous referee whose helpful suggestions have improved the quality of the paper. HK acknowledges a studentship from the Science and Technology Facilities Council (STFC) in the United Kingdom. WCGH acknowledges support from STFC. LJT acknowledges support from the University of Southampton Mayflower scholarship.

REFERENCES

- Alpar, M.A., Cheng, A.F., Ruderman, M.A. & Shaham, J., 1982, *Nature*, 300, 728.
- Becker, P.A., et al., 2012, *A&A*, 544, A123.
- Bird, A. J., Coe, M. J., McBride, V. A. & Udalski, A., 2012, *MNRAS*, 423, 3663.
- Bozzo, E., Falanga, M., & Stella, L., 2008, *AJ*, 683, 1031.
- Chashkina, A. & Popov, S.B, 2012, *New Astron.*, 17, 594.

BeXB	P (s)	\dot{P} (s yr ⁻¹)	L (10 ³⁷ erg s ⁻¹)	B from CRSF (10 ¹² G)	B from GL (10 ¹² G)	Height from GL (km)	Height from B+12 (km)
GRO J1008-57	94	0.25	0.4	9.9	39	5.8	0.3
A0535+26	103	-0.03	0.1	4.3	14 or 0.03	4.8	1.7
RX J0440.9+4431	205	0.21	0.4	3.2	73	18.3	0.3
1A1118-616	408	-14.52	1.4	4.8	230 or 2.2	26.2	0.1
X Per	837	0.11	0.004	3.3	42	13.5	8.7

Table 4. Galactic BeXB containing neutron stars with measured cyclotron resonance scattering feature (CRSF) and spin period time derivative (see text for references). Also shown are magnetic fields determined using CRSF and the Ghosh and Lamb (GL) model, CRSF accretion column heights if the field predicted by the GL model is the surface field, and heights determined using the model described in Becker et al. (2012) (B+12).

- Coburn, W., Heindl, W.A., Gruber, D.E., Rothschild, R.E., Staubert, R., Wilms, J., Kreykenbohm, I., 2001, *ApJ*, 552, 738.
- Coe, M. J., Edge, W. R. T., Galache, J. L. & McBride, V. A., 2005, *MNRAS*, 356, 502.
- Coe, M.J., McBride, V.A. & Corbet, R.H.D., 2010, *MNRAS*, 401, 252.
- Coe, M.J., et al., 2011, *MNRAS*, 414, 3281.
- Coe, M.J., et al., 2012, *MNRAS*, 424, 282.
- Corbet, R.H.D., 1984, *A&A*, 141, 91.
- Davidson, K., & Ostriker, J.P., 1973, *AJ*, 179, 585.
- DeCesar, M.E., Boyd, P.T., Markwardt, C.B., Pottschmidt, K., Miller, M.C., Ströhmayer, T. E., Suchy, S. & Wilms, J., 2009, *BAAS*, 41, 299.
- de Oliveira, R.L., Motch, C., Haberl, F., Negueruela, I., & Janot-Pacheco, E., 2006, *A&A*, 454, 265.
- Doroshenko, V., Suchy, S., Santangelo, A., Staubert, R., Kreykenbohm, I., Rothschild, R., Pottschmidt, K. & Wilms, J., 2010a, *A&A*, 515, L1.
- Doroshenko, V., Santangelo, A., Suleimanov, V., Staubert, R., Kreykenbohm, I., Ferrigno, C., & Klochkov, D., 2010b, in Comastri A., Angelini L., Cappi M., eds, *AIP Conf. Proc.*, Vol. 1248, X-Ray Astronomy 2009; Present Status, Multi-Wavelength Approach and Future Perspectives. Am. Inst. Phys., New York, 155.
- Galache, J.L., Corbet, R.H.D., Coe, M.J., Laycock, S., Schurch, M.P.E., Markwardt, C., Marshall, F.E. & Lochner, J., 2008, *ApJS*, 177, 189.
- Ghosh, P., & Lamb, F.K., 1979, *AJ*, 234, 296.
- Grimm, H.J., Gilfanov, M. & Sunyaev, R., 2003, *MNRAS*, 339, 793.
- Haberl, F., 1995, *A&A*, 296, 685.
- Heindl, W.A., Coburn, W., Gruber, D.E., Rothschild, R.E., Kreykenbohm, I., Wilms, J. & Staubert, R., 2001, *ApJ*, 563, L35.
- Heindl, W.A., Coburn, W., Kreykenbohm, I. & Wilms, J., 2003, *Astron. Telegram*, 200.
- Ho, W.C.G., Klus, H., Coe, M.J. & Andersson, N., 2013, *MNRAS*, in press (arXiv:1311.1969).
- Illarionov, A.F. & Kompaneets, D.A., 1990, *MNRAS*, 247, 219.
- Illarionov, A.F. & Sunyaev, R.A., 1975, *A&A*, 39, 185.
- Kendziorra, E., et al., 1994, *A&A*, 291, L31.
- Klochkov, D., et al., 2012, *A&A* 542, L28.
- Klus, H., Bartlett, E.S., Bird, A.J., Coe, M.J., Corbet, R.H.D., & Udalski, A., 2013, *MNRAS*, 428, 3607.
- Kluzniak, W., & Rappaport, S., 2007, *AJ*, 671, 1990.
- Lai, D., 1996, *ApJ*, 466, L35.
- Li, X.D., & Van Den Heuvel, E.P.J., 1999, *ApJ*, 513, L45.
- Laycock, S., Corbet, R.H.D., Coe, M.J., Marshall, F.E., Markwardt, C. & Lochner, J., 2005, *ApJS*, 161, 96.
- Lipunov, V.M., 1992, *Astrophysics of Neutron Stars*, Vol. XIII, Springer-Verlag, Berlin.
- McBride, V.A., M.J. Coe, I. Negueruela, I., Schurch, M. P. E. & McGowan, K. E., 2008, *MNRAS*, 388, 1198.
- Maisack, M., Grove, J.E., Kendziorra, E., Kretschmar, P., Staubert, R., Strickman, M.S., 1997, *A&A*, 325, 212.
- Makishima, K., et al., 1990, *ApJ*, 365, L59.
- Manchester, R.N., Hobbs, G.B., Teoh, A., & Hobbs, M., 2005, *AJ*, 129, 1993.
- Mihara, T., Makishima, K., Kamijo, S., Ohashi, T., Nagase, F., Tanaka, Y. & Koyama, K., 1991, *ApJ*, 379, L61.
- Negueruela, I., Okazaki, A.T., 2001, *A&A*, 369, 108.
- Nespoli, E., & Reig, P., 2011, *A&A*, 526, 7.
- Nomoto, K., 1984, *ApJ*, 277, 791.
- Nomoto, K., & Kondo, Y., 1991, *ApJ*, 367, L19.
- Okazaki, A.T., Negueruela, I., 2001, *A&A*, 377, 161.
- Okazaki, A.T., Bate, M.R., Ogilvie, G.I., & Pringle, J.E., *MNRAS*, 337, 967.
- Podsiadlowski, Ph., Langer, N., Poelarends, A.J.T., Rappaport, S., Heger, A., Pfahl, E., 2004, *ApJ*, 612, 1044.
- Pons, J.A., Miralles, J.A. & Geppert, U., 2009, *A&A*, 496, 207.
- Postnov, K., Shakura, N.I, Kochetkova, A., & Hjalmarsdotter, L., 2011, *Proc. Extreme and Variable High Energy Sky POS (Extremesky 2011)* 017 (<http://pos.sissa.it/cgi-bin/reader/conf.cgi?confid=147#session-4>).
- Poutanen, J., Mushtukov, A.A., Suleimanov, V.F., Tsygankov, S.S., Nagirner, D.I., Doroshenko, V., & Lutovinov, A.A., 2013, *ApJ*, 777, 115.
- Pringle, J.E., 1996, *MNRAS*, 281, 357.
- Pringle, J.E., & Rees, M.J., 1972, *A&A*, 21, 1.
- Rajaelimanana, A. F., Charles, P. A. & Udalski A., 2011, *MNRAS*, 413, 1600.
- Reig, P., 2011, *Ap&SS*, 332, 1.
- Reig, P., Fabregat, J., Coe, M.J., 1997, *A&A*, 322, 193.
- Reig, P., Torrejón, J. M., & Blay, P., 2012, *MNRAS*, 425, 595.
- Reynolds, A.P., Parmar, A.N., & White, N. E., 1993, *ApJ*, 414, 302.
- Santangelo, A., Segreto, A., Giarrusso, S., Dal Fiume, D., Orlandini, M., Parmar, A.N., Oosterbroek, T., et al., 1999, *ApJ*, 523, L85.
- Schmidtke, P. C., Cowley, A. P. & Udalski, A., 2006, *AJ*, 132, 919.
- Schurch, M. P. E., 2009, *Doctoral dissertation*, Univ. Southampton.
- Schurch, M., Udalski, A. & Coe, M.J., 2008, *Astron. Tele-*

gram, 1670.

Shakura, N., Postnov, K., Kochetkova, A., & Hjalmarsdotter, L., 2012, MNRAS, 420, 216.

Shapiro, S.L. & Lightman, A.P., 1976, ApJ, 204, 555.

Shrader, C.R., Sutaria, F.K., Singh, K.P. & Macomb, D.J., 1991, ApJ, 512, 920.

Shvartsman V.F., 1970, Radiofizika, 13, 1852.

Stanimirović, S., Staveley-Smith, L., Dickey, J.M., Sault, R.J., & Snowden, S.L., 1999, MNRAS, 302, 417.

Staubert, R., Shakura, N., Postnov, K., Wilms, J., Rothschild, R., Coburn, W., Rodina, L. & Klochkov, D., 2007, A&A, 465, L25.

Sturm, R., Haberl, F., Pietsch, W., Coe, M.J., Mereghetti, S., La Palombara, N., Owen, R.A. & Udalski, A., 2012, A&A, 537, 76.

Taam, R.E., & van den Heuvel, E.P.J., 1986, ApJ, 305, 235.

Townsend L.J., Corbet, R.H.D., Coe, M.J., McBride, V.A., Hill, A.B. & Bird A.J., 2009, Astron. Telegram, 2202.

Townsend, L.J., Coe, M.J., Corbet, R.H.D., McBride, V.A., Hill, A.B., Bird, A.J. & Schurch, M.P.E. et al., 2011b, MNRAS, 410, 1813.

Townsend, L.J., Coe, M.J., Corbet, R.H.D. & Hill, A.B., 2011a, MNRAS, 416, 1556.

Townsend, L.J., Drave, S.P., Hill, A.B., Coe, M.J., Corbet, R.H.D. & Bird, A. J., 2013, MNRAS, 433, 23.

Tsygankov, S.S., Krivonos, R.A. & Lutovinov, A.A., 2012, MNRAS, 421, 2407.

Wang, Y.M., 1981, A&A, 102, 36.

APPENDIX A: DERIVATION OF ANGULAR MOMENTUM OF ACCRETING MATTER

For a neutron star accreting from a companion, two cases have previously been considered: accretion via Roche lobe overflow or accretion via a stellar wind. For Roche lobe overflow, accreting matter has high angular momentum and therefore easily forms an accretion disc around the neutron star. In the case of a stellar wind, matter has low angular momentum and therefore accretion likely occurs spherically (Illarionov & Sunyaev 1975; Shapiro & Lightman 1976). We consider a third case: accretion from a circumstellar disc around an OBe main sequence companion at periastron passage. We follow closely the derivation from Shapiro & Lightman (1976) (see also Wang 1981) of the angular momentum of the accreting matter, bearing in mind that the work of Shapiro & Lightman is for matter from a radially outflowing wind, while our case is a wind that (1) is moving tangentially to the direction of the companion and (2) has a Kelperian velocity gradient with distance from the companion.

When the neutron star enters the circumstellar disc, the star forms an accretion cylinder of radius R_B . If there is no density or velocity gradient in the wind, then there is no net angular momentum transferred due to symmetry, i.e. spin up on one side and spin down on the other. However, since the density and velocity decrease as a function of distance, e.g.,

$$\rho = \rho_0 R_{cd}^{-n_\rho}, \quad (\text{A1})$$

there will be a net angular momentum change due to accretion.

Let us consider a cross-section of the accretion cylinder, which defines the xy -plane, with radius R_B . The angular momentum passing through this plane $dx dy$ is

$$dJ = (\rho dx dy V_{rel} dt) V_{rel} y = \rho y V_{rel}^2 dx dy dt, \quad (\text{A2})$$

where y is the radial distance from the cylinder axis. We examine the first-order density and velocity perturbation about the periastron separation a , i.e.,

$$\rho(x, y) \approx \rho(a) + \left. \frac{d\rho}{dR_{cd}} \right|_a y = \rho(a) \left(1 - n_\rho \frac{y}{a} \right) \quad (\text{A3})$$

$$V_{rel}(x, y) \approx V_{rel}(a) + \left. \frac{dV_{rel}}{dR_{cd}} \right|_a y = V_{rel}(a) \left(1 - \frac{y}{2a} \right). \quad (\text{A4})$$

Note that the dV_{rel}/dR_{cd} term accounts for both the gradient in disc velocity and neutron star orbital velocity. Substituting back into the angular momentum equation we obtain

$$\frac{dJ}{dt} = \rho(a) y V_{rel}(a)^2 dx dy \left[1 - \left(n_\rho + \frac{1}{2} \right) \frac{y}{a} \right]. \quad (\text{A5})$$

The net angular momentum transferred per unit mass is then found by integrating dJ/dt over the accretion cylinder and dividing by the mass accretion rate where $\dot{M} = \pi R_B^2 \rho V_{rel}$, i.e.,

$$\begin{aligned} J &= \frac{\rho V_{rel}^2}{\pi R_B^2 \rho V_{rel}} \int y [1 - (n_\rho + 1/2)(y/a)] dx dy \\ &= -\frac{1}{4} (n_\rho + 1/2) V_{rel} \frac{R_B^2}{a}. \end{aligned} \quad (\text{A6})$$

We also consider the case where the neutron star truncates the radial extent of the circumstellar disc. If matter only occupies the hemisphere closest to the companion, then we find

$$\begin{aligned} J_t &= \frac{V_{rel}}{\pi R_B^2} \int_\pi^{2\pi} \int_0^{R_B} [1 - (n_\rho + 1/2)(R_{cd} \sin \theta/a)] R_{cd}^2 \sin \theta dr d\theta \\ &= -V_{rel} R_B \left[\frac{2}{3\pi} + \frac{1}{8} (n_\rho + 1/2) \frac{R_B}{a} \right]. \end{aligned} \quad (\text{A7})$$

APPENDIX B: PLOTS OF P AND L VS MJD

Figs B1-B42 show plots of spin period (upper panel) and luminosity (lower panel) as functions of MJD for the 42 systems in our data set. The weighted line of best-fit, used to determine the long-term average \dot{P} , is calculated using MP-FITEXPR (see Section 2).

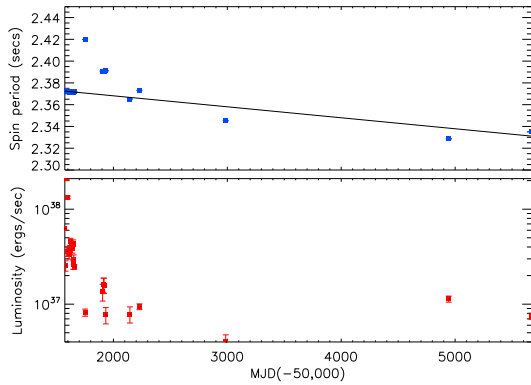


Figure B1. The upper panel shows spin period as a function of MJD and the lower panel shows luminosity as a function of MJD for the source SXP2.37. The line in the upper panel shows the best-fitting \dot{P} .

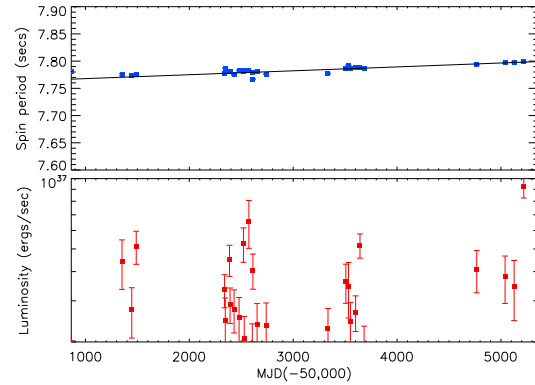


Figure B4. The upper panel shows spin period as a function of MJD and the lower panel shows luminosity as a function of MJD for the source SXP7.78. The line in the upper panel shows the best-fitting \dot{P} .

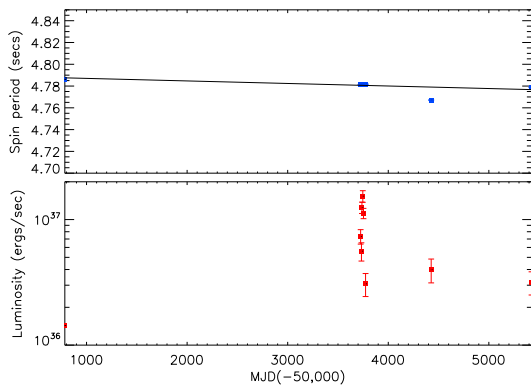


Figure B2. The upper panel shows spin period as a function of MJD and the lower panel shows luminosity as a function of MJD for the source SXP4.78. The line in the upper panel shows the best-fitting \dot{P} .

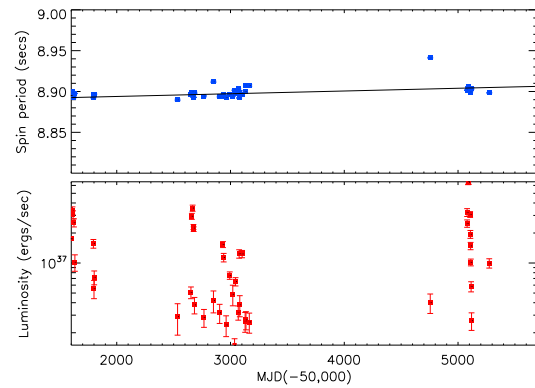


Figure B5. The upper panel shows spin period as a function of MJD and the lower panel shows luminosity as a function of MJD for the source SXP8.80. The line in the upper panel shows the best-fitting \dot{P} .

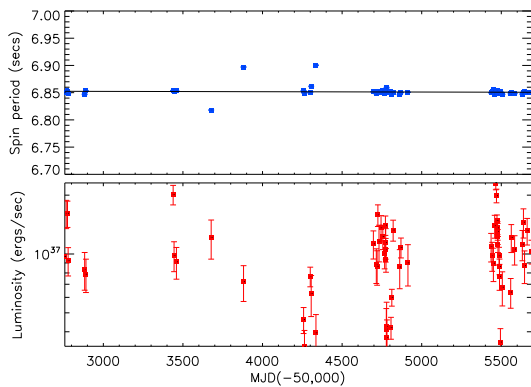


Figure B3. The upper panel shows spin period as a function of MJD and the lower panel shows luminosity as a function of MJD for the source SXP6.85. The line in the upper panel shows the best-fitting \dot{P} .

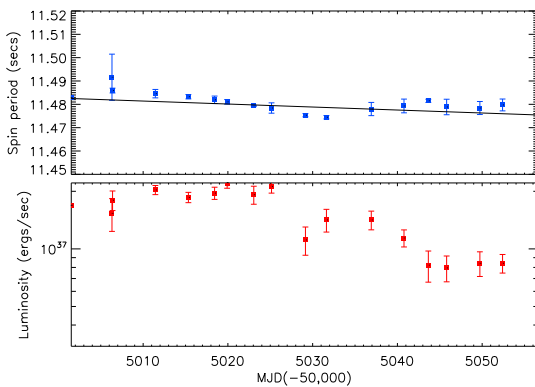


Figure B6. The upper panel shows spin period as a function of MJD and the lower panel shows luminosity as a function of MJD for the source SXP11.5. The line in the upper panel shows the best-fitting \dot{P} .

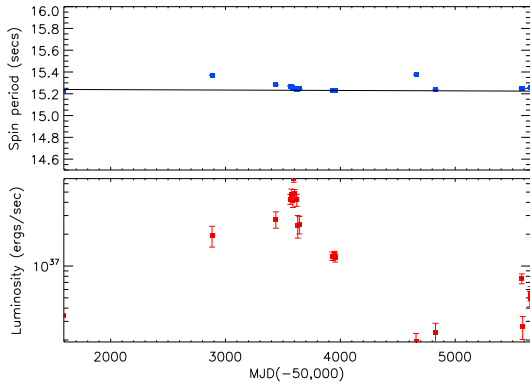


Figure B7. The upper panel shows spin period as a function of MJD and the lower panel shows luminosity as a function of MJD for the source SXP15.3. The line in the upper panel shows the best-fitting \dot{P} .

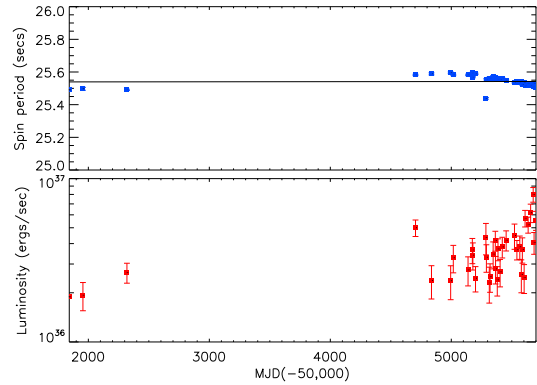


Figure B10. The upper panel shows spin period as a function of MJD and the lower panel shows luminosity as a function of MJD for the source SXP25.5. The line in the upper panel shows the best-fitting \dot{P} .

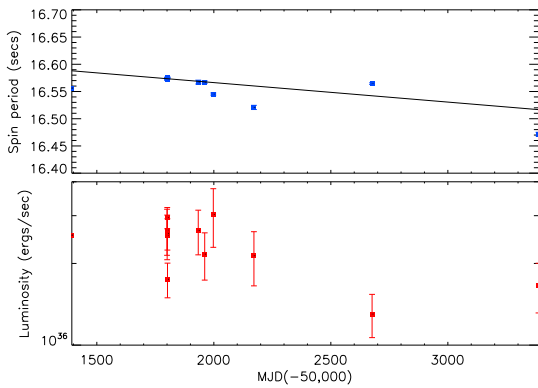


Figure B8. The upper panel shows spin period as a function of MJD and the lower panel shows luminosity as a function of MJD for the source SXP16.6. The line in the upper panel shows the best-fitting \dot{P} .

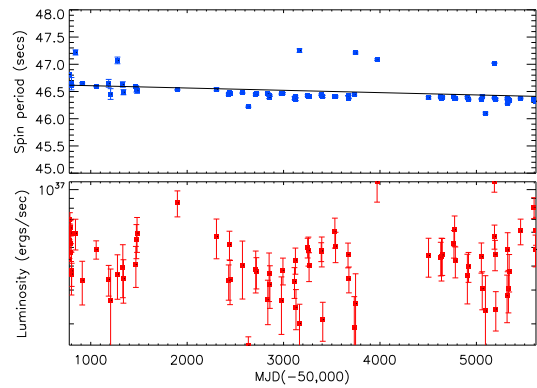


Figure B11. The upper panel shows spin period as a function of MJD and the lower panel shows luminosity as a function of MJD for the source SXP46.6. The line in the upper panel shows the best-fitting \dot{P} .

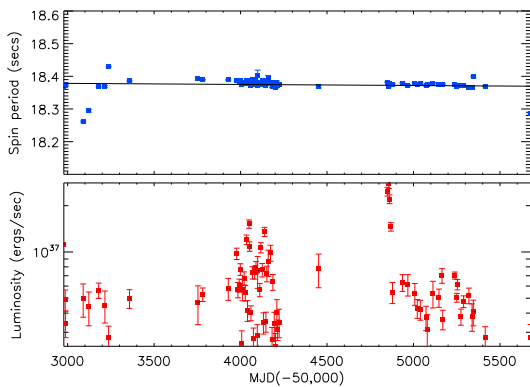


Figure B9. The upper panel shows spin period as a function of MJD and the lower panel shows luminosity as a function of MJD for the source SXP18.3. The line in the upper panel shows the best-fitting \dot{P} .

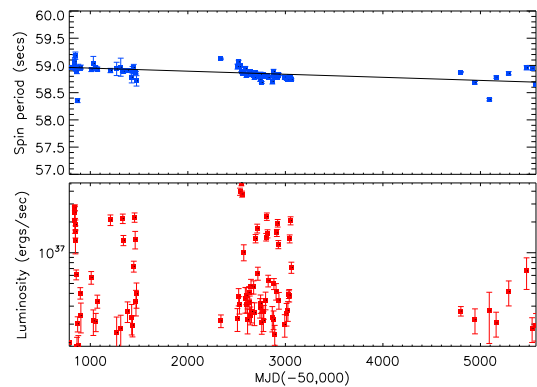


Figure B12. The upper panel shows spin period as a function of MJD and the lower panel shows luminosity as a function of MJD for the source SXP59.0. The line in the upper panel shows the best-fitting \dot{P} .

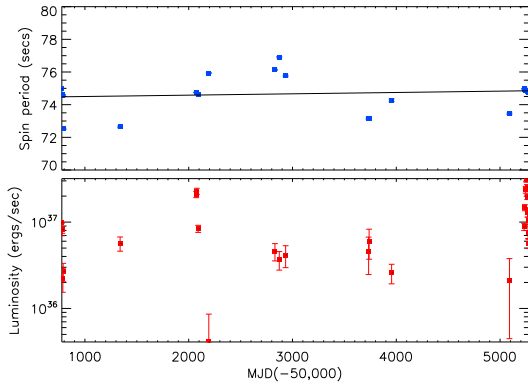


Figure B13. The upper panel shows spin period as a function of MJD and the lower panel shows luminosity as a function of MJD for the source SXP74.7. The line in the upper panel shows the best-fitting \dot{P} .

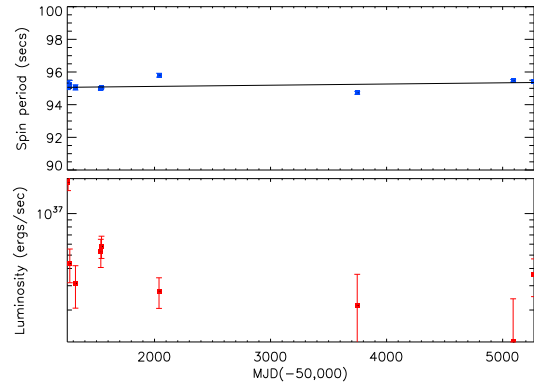


Figure B16. The upper panel shows spin period as a function of MJD and the lower panel shows luminosity as a function of MJD for the source SXP95.2. The line in the upper panel shows the best-fitting \dot{P} .

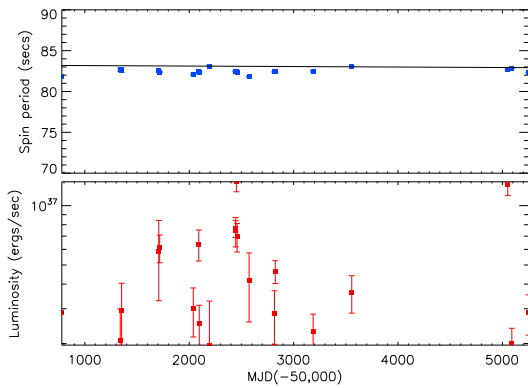


Figure B14. The upper panel shows spin period as a function of MJD and the lower panel shows luminosity as a function of MJD for the source SXP82.4. The line in the upper panel shows the best-fitting \dot{P} .

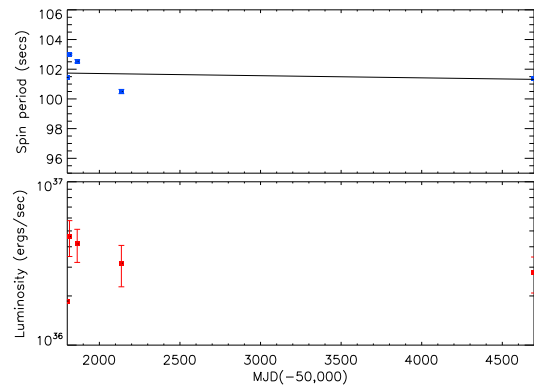


Figure B17. The upper panel shows spin period as a function of MJD and the lower panel shows luminosity as a function of MJD for the source SXP101. The line in the upper panel shows the best-fitting \dot{P} .

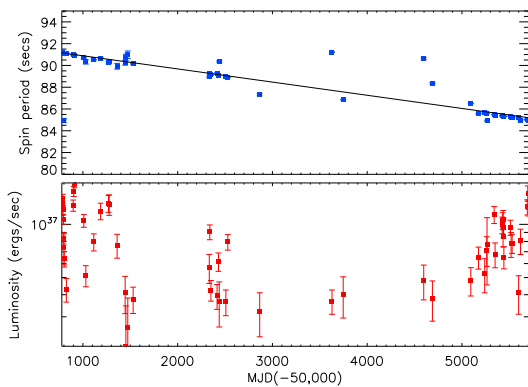


Figure B15. The upper panel shows spin period as a function of MJD and the lower panel shows luminosity as a function of MJD for the source SXP91.1. The line in the upper panel shows the best-fitting \dot{P} .

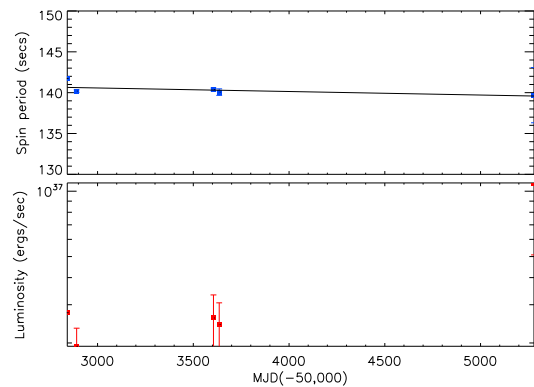


Figure B18. The upper panel shows spin period as a function of MJD and the lower panel shows luminosity as a function of MJD for the source SXP140. The line in the upper panel shows the best-fitting \dot{P} .

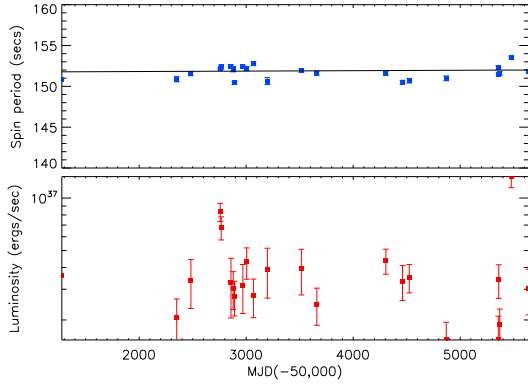


Figure B19. The upper panel shows spin period as a function of MJD and the lower panel shows luminosity as a function of MJD for the source SXP152. The line in the upper panel shows the best-fitting \dot{P} .

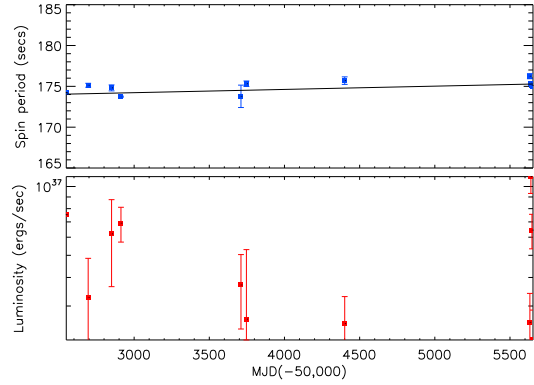


Figure B22. The upper panel shows spin period as a function of MJD and the lower panel shows luminosity as a function of MJD for the source SXP175. The line in the upper panel shows the best-fitting \dot{P} .

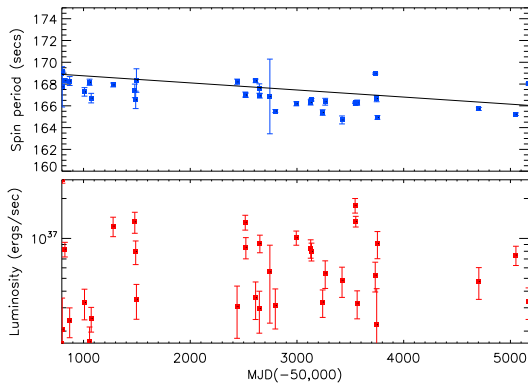


Figure B20. The upper panel shows spin period as a function of MJD and the lower panel shows luminosity as a function of MJD for the source SXP169. The line in the upper panel shows the best-fitting \dot{P} .

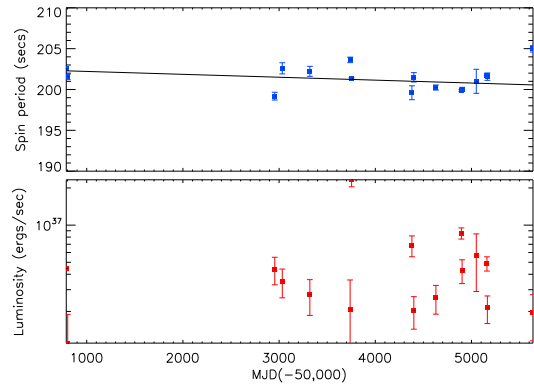


Figure B23. The upper panel shows spin period as a function of MJD and the lower panel shows luminosity as a function of MJD for the source SXP202A. The line in the upper panel shows the best-fitting \dot{P} .

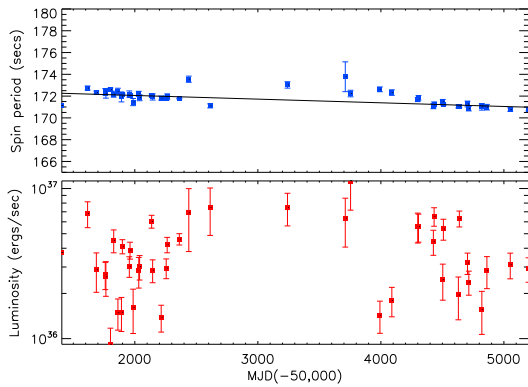


Figure B21. The upper panel shows spin period as a function of MJD and the lower panel shows luminosity as a function of MJD for the source SXP172. The line in the upper panel shows the best-fitting \dot{P} .

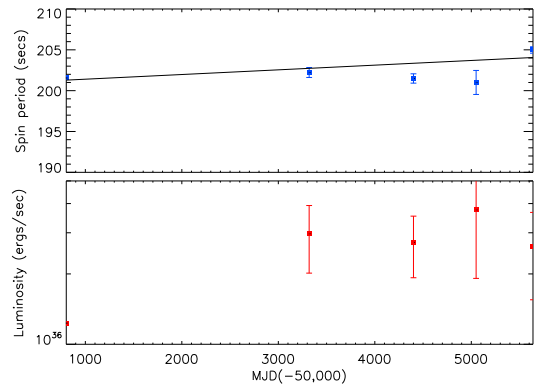


Figure B24. The upper panel shows spin period as a function of MJD and the lower panel shows luminosity as a function of MJD for the source SXP202B. The line in the upper panel shows the best-fitting \dot{P} .

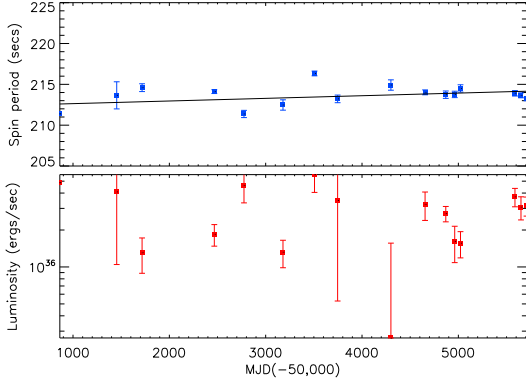


Figure B25. The upper panel shows spin period as a function of MJD and the lower panel shows luminosity as a function of MJD for the source SXP214. The line in the upper panel shows the best-fitting \dot{P} .

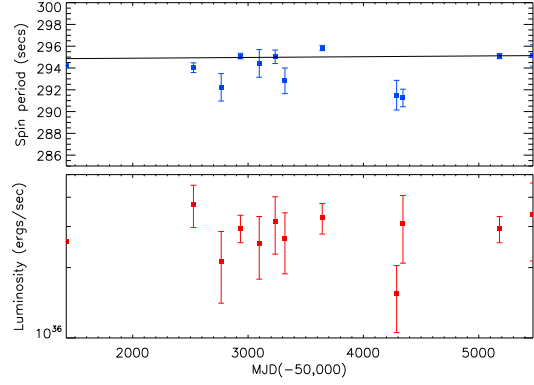


Figure B28. The upper panel shows spin period as a function of MJD and the lower panel shows luminosity as a function of MJD for the source SXP293. The line in the upper panel shows the best-fitting \dot{P} .

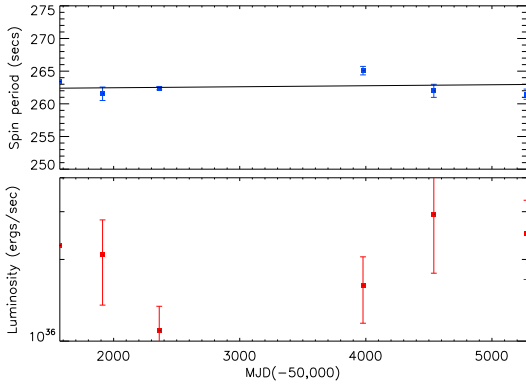


Figure B26. The upper panel shows spin period as a function of MJD and the lower panel shows luminosity as a function of MJD for the source SXP264. The line in the upper panel shows the best-fitting \dot{P} .

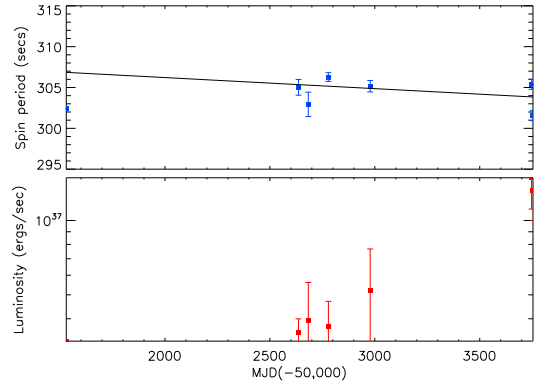


Figure B29. The upper panel shows spin period as a function of MJD and the lower panel shows luminosity as a function of MJD for the source SXP304. The line in the upper panel shows the best-fitting \dot{P} .

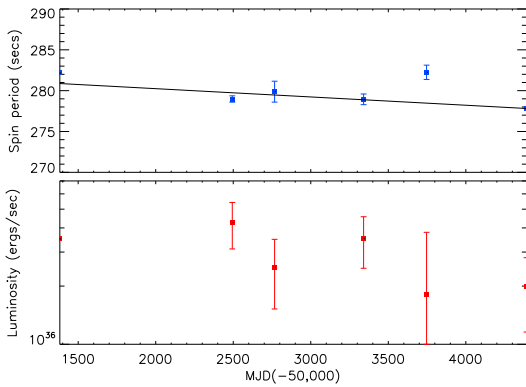


Figure B27. The upper panel shows spin period as a function of MJD and the lower panel shows luminosity as a function of MJD for the source SXP280. The line in the upper panel shows the best-fitting \dot{P} .

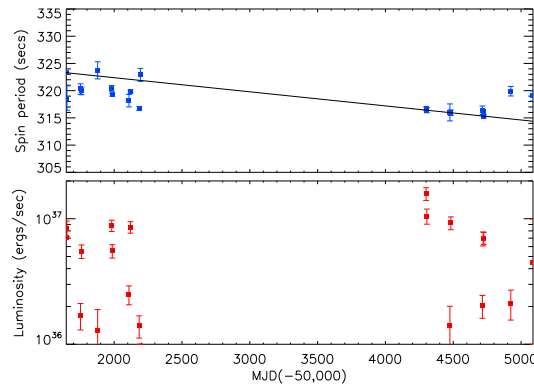


Figure B30. The upper panel shows spin period as a function of MJD and the lower panel shows luminosity as a function of MJD for the source SXP323. The line in the upper panel shows the best-fitting \dot{P} .

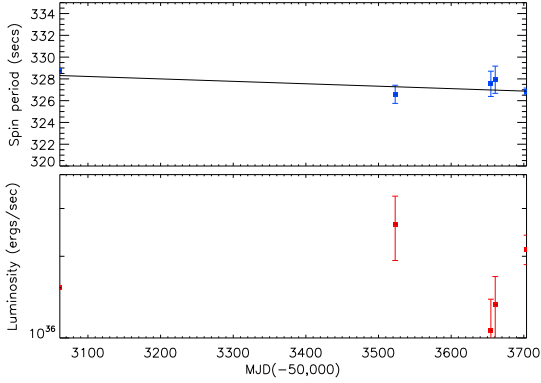


Figure B31. The upper panel shows spin period as a function of MJD and the lower panel shows luminosity as a function of MJD for the source SXP327. The line in the upper panel shows the best-fitting \dot{P} .

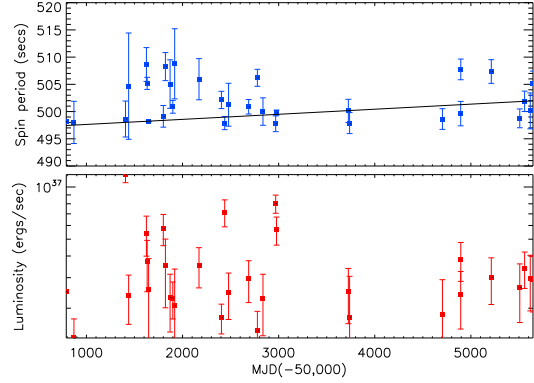


Figure B34. The upper panel shows spin period as a function of MJD and the lower panel shows luminosity as a function of MJD for the source SXP504. The line in the upper panel shows the best-fitting \dot{P} .

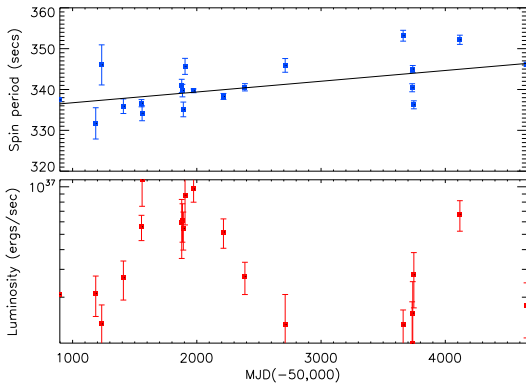


Figure B32. The upper panel shows spin period as a function of MJD and the lower panel shows luminosity as a function of MJD for the source SXP342. The line in the upper panel shows the best-fitting \dot{P} .

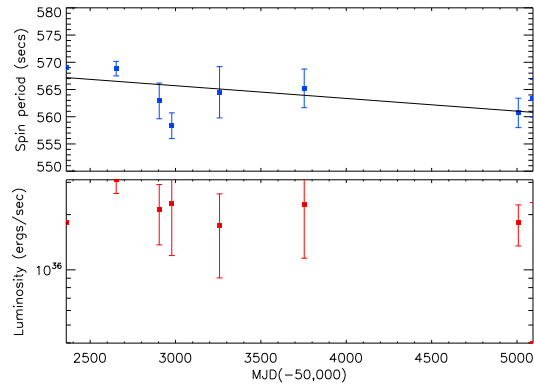


Figure B35. The upper panel shows spin period as a function of MJD and the lower panel shows luminosity as a function of MJD for the source SXP565. The line in the upper panel shows the best-fitting \dot{P} .

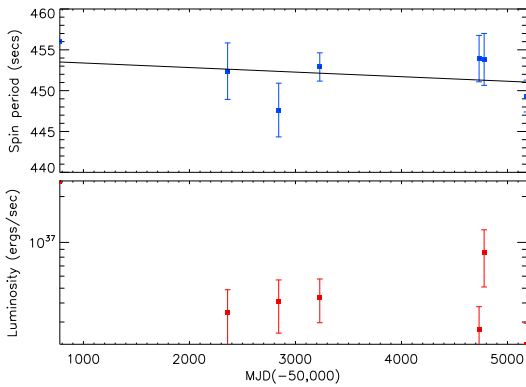


Figure B33. The upper panel shows spin period as a function of MJD and the lower panel shows luminosity as a function of MJD for the source SXP455. The line in the upper panel shows the best-fitting \dot{P} .

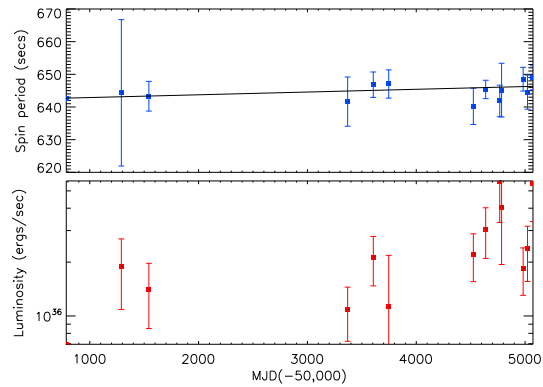


Figure B36. The upper panel shows spin period as a function of MJD and the lower panel shows luminosity as a function of MJD for the source SXP645. The line in the upper panel shows the best-fitting \dot{P} .

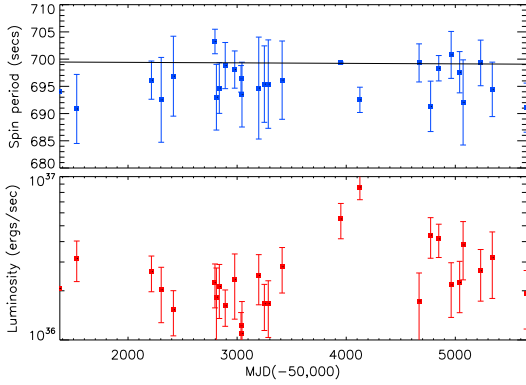


Figure B37. The upper panel shows spin period as a function of MJD and the lower panel shows luminosity as a function of MJD for the source SXP701. The line in the upper panel shows the best-fitting \dot{P} .

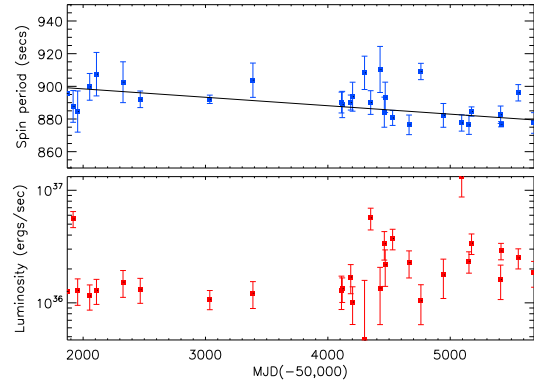


Figure B40. The upper panel shows spin period as a function of MJD and the lower panel shows luminosity as a function of MJD for the source SXP893. The line in the upper panel shows the best-fitting \dot{P} .

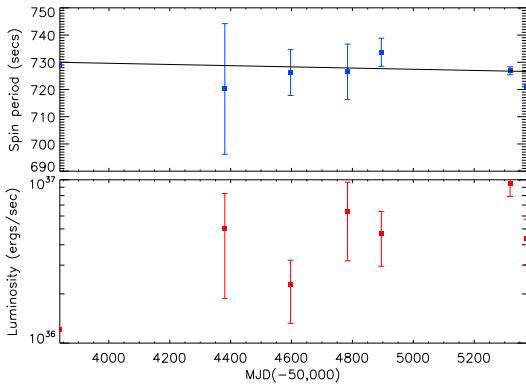


Figure B38. The upper panel shows spin period as a function of MJD and the lower panel shows luminosity as a function of MJD for the source SXP726. The line in the upper panel shows the best-fitting \dot{P} .

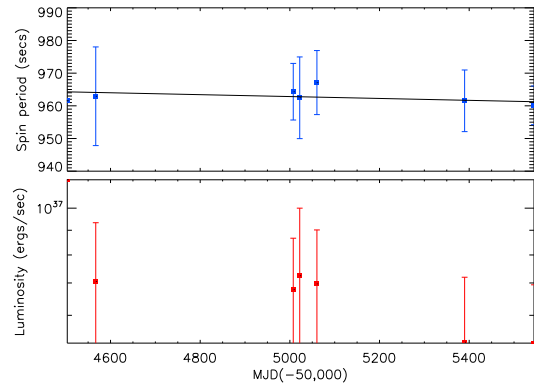


Figure B41. The upper panel shows spin period as a function of MJD and the lower panel shows luminosity as a function of MJD for the source SXP967. The line in the upper panel shows the best-fitting \dot{P} .

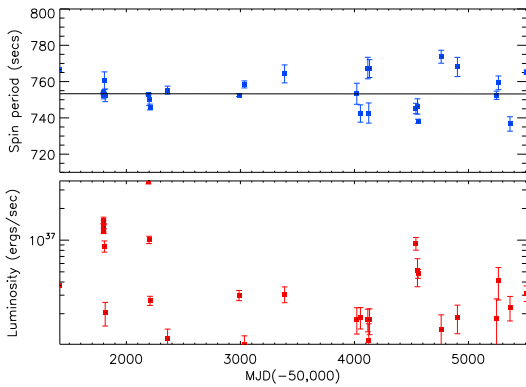


Figure B39. The upper panel shows spin period as a function of MJD and the lower panel shows luminosity as a function of MJD for the source SXP756. The line in the upper panel shows the best-fitting \dot{P} .

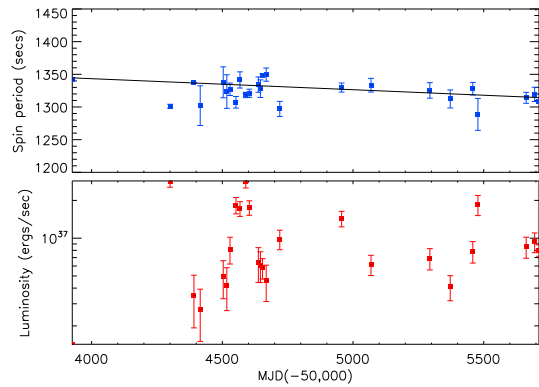


Figure B42. The upper panel shows spin period as a function of MJD and the lower panel shows luminosity as a function of MJD for the source SXP1323. The line in the upper panel shows the best-fitting \dot{P} .